Winter 1-31-2021

Nanoengineered Materials for Energy Conversion & Storage Applications: A Density Functional Theory Study

Ahmed Biby
ahmed.h.biby@aucegypt.edu

The American University in Cairo

School of Science and Engineering

The Nanotechnology Program

Nanoengineered Materials for Energy Conversion & Storage Applications: A Density Functional Theory Study

A Thesis in

Nanotechnology

By

Ahmed Hossameldin Biby

Submitted in Partial Fulfilment

of The Requirements

for The Degree of Masters of Science in Nanotechnology

September 2020

Abstract

The conventional approach for the development of novel materials has become long relative to the desired product development cycle. Thus, the sluggish pace of the development of materials within the conventional approach hinders the rapid transformation of the scientific outcomes into useful technological products. To this end, the field of hierarchical materials informatics evolved to bridge this gap. In this field, the multiscale material internal structure is considered the starting point and the core of this approach. This being said, the density functional theory (DFT) was used to generate useful materials data for the advancement of the hierarchical materials data-bases towards the novel efficient data-driven materials design approach. In this study, the DFT was employed to tackle energy materials arena as the global community is heading towards the renewable energies paradigm to secure the pillars of sustainability. Photoelectrochemical (PEC) water splitting proved to be one of the most trailblazing technologies serving this dazzling aspiration. Development of efficient photoelectrodes through defect engineering of wide-bandgap metal oxides has been the prime focus of materials scientists for decades. However, tuning the properties of m-ZrO_2 was scarcely addressed in the context of photoelectrochemical (PEC) water splitting. In addition, the effect of carbon defects in wide-bandgap metal oxides for PEC applications raised numerous controversies and still elusive. To this end, herein, the effect of various carbon defects in m-ZrO_2 for PEC applications was investigated using the density functional theory to probe the thermodynamic, electronic, and optical properties of the defective structures. The defect formation energies revealed that elevating the temperature promotes and facilitates the formation of carbon defects. Moreover, the binding energies confirmed the stability of all studied complex carbon defects. Furthermore, the band edge positions against the redox potentials of water species exemplified that all the studied defective structures can serve as photoanodes. Additionally, C_{O3c} (carbon atom substituted O_{3c} site) was the only defective structure that exhibited slight straddling of the redox potentials of water species. Importantly, all the defective structures enhanced the light absorption to different extents. Also, it is reported

that $C_{O3c}V_{O3c}$ (carbon atom substituted O_{3c} associated with O_{3c} vacancy) defective m-ZrO_2 enjoyed low direct bandgap (1.9 eV), low defect formation energy, low exciton binding energy, high mobility of charge carriers, fast charge transfer, and low recombination rate. Concurrently, its optical properties were excellent in terms of high absorption, low reflectivity and improved static dielectric constant. Hence, the study recommends $C_{O3c}V_{O3c}$ defective m-ZrO_2 as the leading candidate defective structure to serve as a photoanode for PEC applications. Also, DFT was used to investigate the performance of energy storage electrodes. The DFT proved to be a reliable tool for investigating the quantum capacitance performance of the EDL supercapacitor electrodes. DFT was used to give insights on the capacitance performance of graphene, graphite, carbon nanotubes (CNTs), and N-doped graphene. The results revealed that the quantum capacitance of the CNTs was very high in both positive and negative potential windows and that the N-doping greatly enhanced the capacitance performance of the pristine graphene.

The thesis of Ahmed Hossameldin Biby was reviewed and approved*by the following:

Nageh K. Allam

Professor, The American University in Cairo.

Director, Nanotechnology Program.

Director, Energy of Materials Laboratory (EML).

Thesis Advisor

Chair of Committee

Ahmed Hamed

Assistant Professor, Department of Physics.

The American University in Cairo.

Internal Examiner

Ahmed El-Nahas

Professor, Department of Chemistry.

Menoufia University.

External Examiner

Mohamed Orabi

Assistant Professor, Department of Physics.

The American University in Cairo.

Thesis moderator

*Signatures are on file in the Graduate School.

Table of Contents

LIST OF FIGURES

LIST OF TABLES

LIST OF ACRONYMS

CA-PZ	*Ceperley-Alder-Perdew-Zunger*
CASTEP	*Cambridge Serial Total Energy Package*
CB	*Conduction Band*
CBM	*Conduction Band Minimum*
CNTs	*Carbon Nanotubes*
DFT	*Density Functional Theory*
DOS	*Density Of States*
EDL	*Electrical Double Layer*
FLL	*Fully Localized Limit*
GGA	*Generalized Gradient Approximation*
HER	*Hydrogen Evolution Reaction*
HF	*Hartree-Fock*
KS	*Kohn-Sham*
LDA	*Local Density Approximation*
LSD	*Local Spin Density*
NDG	*Nitrogen-Doped Graphene*
NEB	*Nudged Elastic Band*
OER	*Oxygen Evolution Reaction*
PAW	*Projector Augmented-Wave*
PBE	*Perdew–Burke-Ernzerhof*
PDOS	*Partial Density Of States*
PEC	*Photoelectrochemical*
PSP	*Process-Structure-Property*
PV-EC	*Photovoltaic-Electrochemical*
PZC	*Potential of Zero Charge*
QC	*Quantum Capacitance*
RHE	*Reference Hydrogen Electrode*
SC	*Semiconductor*
SIESTA	*Spanish Initiative for Electronic Simulations with Thousands of Atoms*
STH	*Solar-To- Hydrogen*
TDOS	*Total Density Of States*
VASP	*Vienna Ab-initio Simulation Package*

VB	*Valence Band*
VBM	*Valence Band Maximum*
VdW	*Van Der Waals*
XC	*Exchange-Correlation*

ACKNOWLEDGEMENTS

All praise is due to Allah. We praise Him, seek for His assistance and forgiveness and we seek refuge with Him from evils of our souls and our misdeeds. No one can mislead whosoever Allah guides and none can guide whosoever Allah causes to go astray. And as our Prophet (ﷺ) said: "He who does not thank people does not thank Allah" we shall abide and obey. This being said, I am utterly grateful and thankful to all who supported and guided me through the journey of the masters degree. A special appreciation goes to my father and my mother (may allah grant them jannah tul Firdous) who backed me heart and soul throughout my life in each and every single aspect of life with hearts full of unconditional love; they literally sacrificed everything to make me the way who I am now. Comes second to my parents is the support of my beloved wife who brightened up my life from day one of our marriage. She was always there for me, helped me a lot in my research and writing the thesis was not possible without her support and encouragement. Her persistent positivity and brilliant academic and social ideas made my life easier, full of hope and optimism. Also, I thank my lovely sister for her support and care. For my son Al-Baraa, I would like to thank him for his endurance during my thesis writing period.

I would like to thank Prof. Nageh for being my mentor and advisor. Since I joined the Energy Materials Laboratory (EML), Prof. Nageh guided and taught me how to be a researcher. His guidance and support went beyond academia to enlighten my personal and social life. Indeed, he was and will always be a caring big brother beside being a dedicated, professional, bright, and an inspiring role-model scientist and advisor; despite all of the hardships that face any researcher in the MENA region. I would also thank Dr. Moustafa Youssef for his efforts in my training on the different ab-initio platforms and their post-treatments. Also, the role and the support of my brothers and colleagues in the EML is invaluable. I also want to thank all the instructors who taught me the graduate courses and the AUC employees who facilitated the administrative work. Finally, I want to thank Al-Ghurair Foundation and the AUC for their financial support during my graduate studies period.

DEDCATION

I dedicate this thesis to my mother and my father.

Chapter I : Introduction

Throughout ages, the technological outcomes of a given era or a specific civilization are linked to the available materials such as the bronze age. From the industrial age till now, the materials are the corner-stone for every development in all of the economic sectors. However, nowadays, the pace of life is faster and the market requirements are ever growing in terms of the endless need for improvement of quality of life on the individual level and securing of resources and welfare of the people on the global level. In this regard, the conventional approach for the development of novel materials has become long relative to the desired product development cycle. Thus, the sluggish pace of the development of materials hinders the rapid transformation of the scientific outcomes into useful technological products. To this end, the field of hierarchical materials informatics evolved to bridge this gap [1]. In this field, the multiscale material internal structure is considered the starting point and the core of this approach as shown in **Figure I-1** [1]. Where each point in the process space represents hybrid process path made up from an ordered sequence of materials manufacturing processes, each point in the structure space refer to a feasible material internal structure, and each point in the properties space represent a physical property of material that can be directly related to the needed function of the material in a given application. Furthermore, hierarchical materials informatics seek to establish process-structure-property (PSP) linkages through reduced-order representations of data science rather than the isolate-and-study approach that was systematic, expensive, and time-consuming**.**

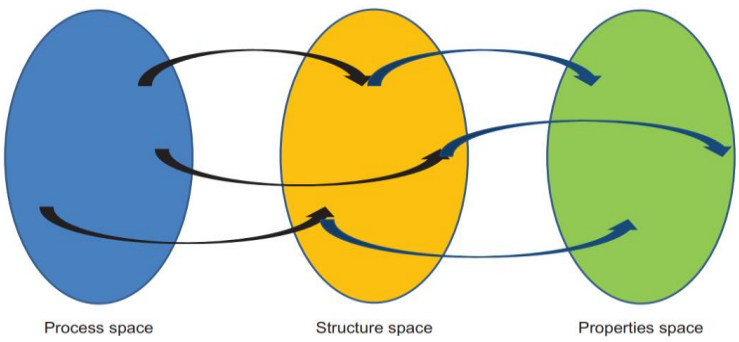

Figure I-1 PSP linkages.

The main challenge in the development of materials within the hierarchical materials informatics approach is the identification of the salient microstructure (multiscale material internal structure) features that are significant to each engineering and technological application [1]. For example, **Figure I-2** [2] shows the different levels needed to asses and analyse a given aircraft structure damage together with the corresponding fundamental science that serve each level of analysis [2].

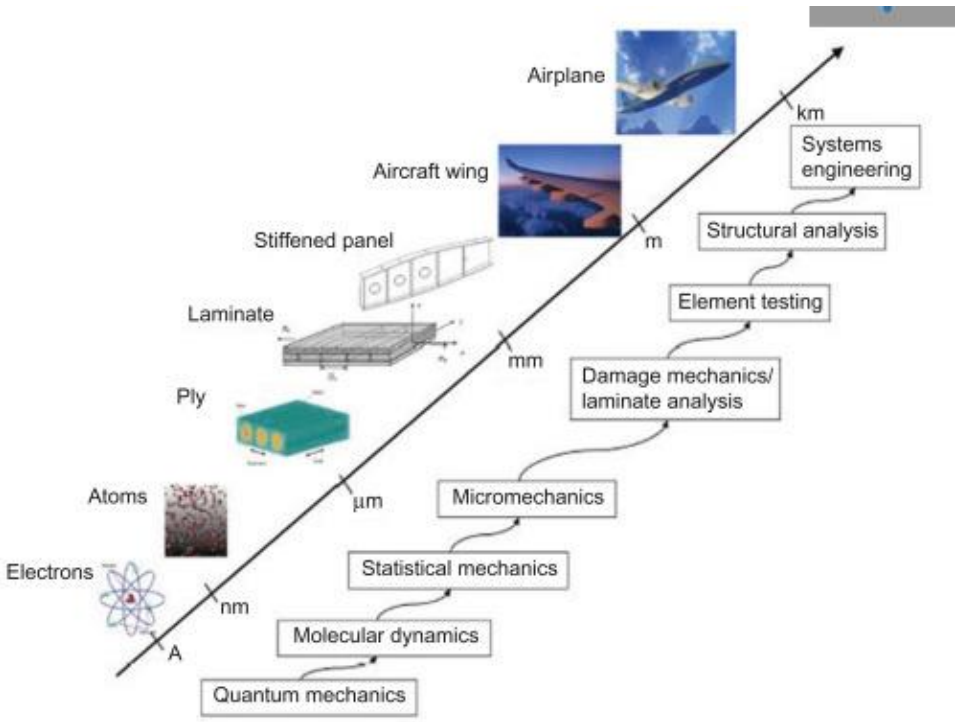

Figure I-2 Various level of analysis for aircraft structure damage.

In this study, the focus would be on the use of quantum-mechanics-based modelling and simulation of materials to treat some key aspects of specific energy materials related to the energy conversion and energy storage. This study adopts the density functional theory (DFT) as the first-principles method to investigate various material properties from the atomic scale point-of-view [3]. DFT is capable of predicting many properties of any atomic system, and proved to be credible and efficient in diverse applications [4–10.] Thanks to the predictive power of the first-principles and the increased available computational resources, DFT has lent itself to the development of high-throughput computational materials studies [11,12]. Hence, this study actively contributes to the advancement of the hierarchical materials data-bases towards the novel efficient data-driven materials design approach.

1.1 Energy Crisis

From the time the humankind discovered fire till now, their dependence on energy is growing and expanding from merely life maintenance activities up to the welfare, entertainment and extravagancy. Although our heavy utilization of energy started since the onset of the industrial age in the mid of the 18th century that marked a major turning point; when the machine took over rather than the hand production methods and domesticated animals and plants [13]. Powered by the capitalist economy and worldview, the world overconsumed the resources of the earth with unprecedented rates aiming at improving the standard of living for the general population. Furthermore, at the level of countries and political alliances, securing the superiority and dominance of the world's economy has been always the prime motive and driver for the geopolitical dynamics. In a capitalist world, the concept of scarcity of resources is the core of capitalism [14]. Therefore, in order for the countries to be in a good economic status; countries strive to secure their proliferating energy demands either by warfare and controlling the territories rich in energy resources (politically or militarily) or throughout peaceful research and development. In addition, humanity is on the verge of facing serious crises that threatens the future of mankind's existence and the living conditions on the globe. Other than energy, the crises are population, food, climate change and natural resources (water, forests, fauna, flora,..etc.). All of them are interconnected in such a way that solving one of them will most probably amplify other(s) or impose a negative impact(s) on another by indirect way, unless it is a sustainable solution [15]. Nowadays, the world mainly relies on fossil fuels as the primary energy source to run their economies. According to the International Energy Agency, the trajectory of energy demand will increase drastically by 40 % from 2009 to 2035. Unfortunately, the utilization of fossil fuels yields combustion products namely; carbon dioxide and other pollutants. It should be noted that carbon dioxide is a greenhouse gas which is the main cause of global warming. Moreover, fossil fuels are non-renewable resources of energy. In conclusion, humanity is confronting two contradicting energy challenges; first, the economic growth and welfare which requires incremental demand of energy and second, mitigating global

warming which necessitates reducing the greenhouse gases emissions, i.e; decreasing the dependence on fossil fuels [15].

1.2 Fossil fuel alternatives

Historically, the conventional energy sources differed and changed at different times. First, wood was used as the primary energy source. Then by the late middle ages, the coal took over. There were also other fuels that were used heavily like the whale oil. It was not until the middle of the 19th century when crude oil became the most dominant type of fuels [16]. From that day, scientists and engineers did not bother themselves to seek seriously for fossil fuel alternatives till war of yom kippur when Arabs reduced the exported oil to the western world in order to limit the interference and the support of the western world to the alleged state of Israel [17]. After this turmoil, the world directed intensive efforts and allocated huge funds towards finding fossil fuel alternatives. Renewable energies such as wind energy, solar energy, geothermal energy, hydroenergy, bioenergy, tidal and waves energy are among the investigated energy resources. Renewable energies have several advantages that relatively differ from one energy to another. Among the merits are the environmental compatibleness, availability and abundance [16]. However, renewable resources have many difficulties that hinder their exploitation and their fossil fuel replacement potential. Herein, only the technical and environmental barriers will be stated. First, the renewable energies suffer from the intermittency. Second, renewable energies are dilute and fluctuating. Third, some of the renewable resources are found in stringent environments such as the geothermal energy. Fourth, utilization of some types of renewables may lead to negative impacts on the ecosystems such as the threatens that wind turbine blades impose on the immigrant birds and the burning of birds passing through the concentrated solar fields [18]. Therefore, renewables need a lot of supporting technologies, e.g: energy storage technologies; to improve its functionality, adequacy and candidacy for the replacement of fossil-fuel-based economy. On the other hand, nuclear energy is a second alternative to fossil fuels yet, it has very high technological barrier and its utilization

is full of safety and security issues which render it exclusive for the developed countries [16]. **Figure I-3** [19] shows the energy demand in 2040 and the potential of various resources to supply energy.

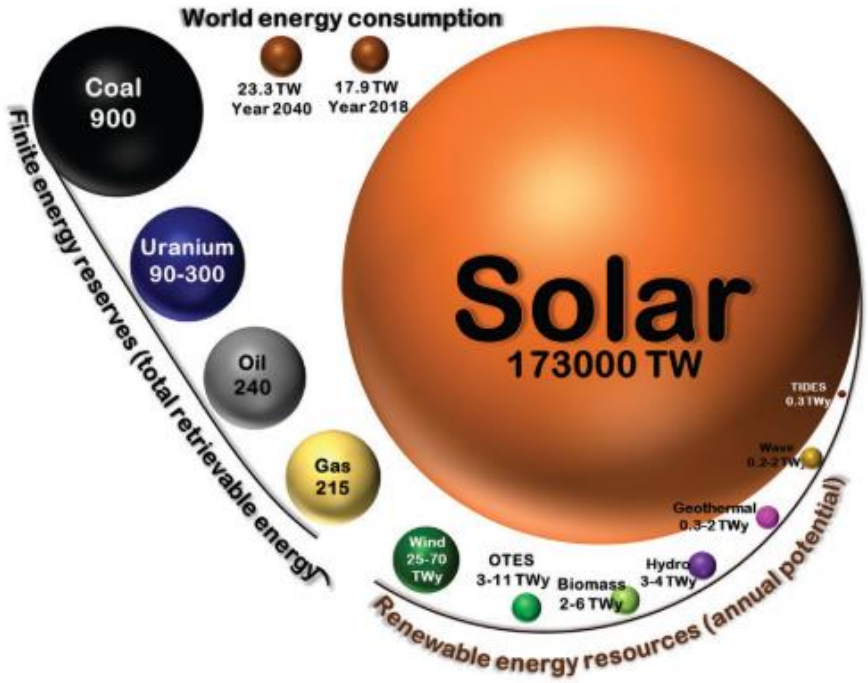

Figure I-3 The projected energy demand in 2040 and the potential of various resources to supply energy.

1.3 Hydrogen economy

Hydrogen is anticipated to be one of the main propellers for the future economy. Hydrogen can be used for energy storage which is a huge advantage for the renewables. Also, hydrogen can be utilized for running the means of transportation. In fact, Hydrogen is a clean-burning fuel, carbon-free and abundant as well as it is nontoxic and environmentally friendly. Moreover, hydrogen is very versatile in its utilization as hydrogen can be liquified, transported and stored. Further, hydrogen can be exploited by aviation, motor cars, industrial enterprises, households and power stations as shown in **Figure I-4** [20]. Fortunately, hydrogen can be produced from electrolysis of water, pyrolysis of natural gas and steam reforming of

hydrocarbons [16]. Sustainably, Hydrogen can be generated from water splitting with the aid of various energies as shown in **Figure I-5** [21].

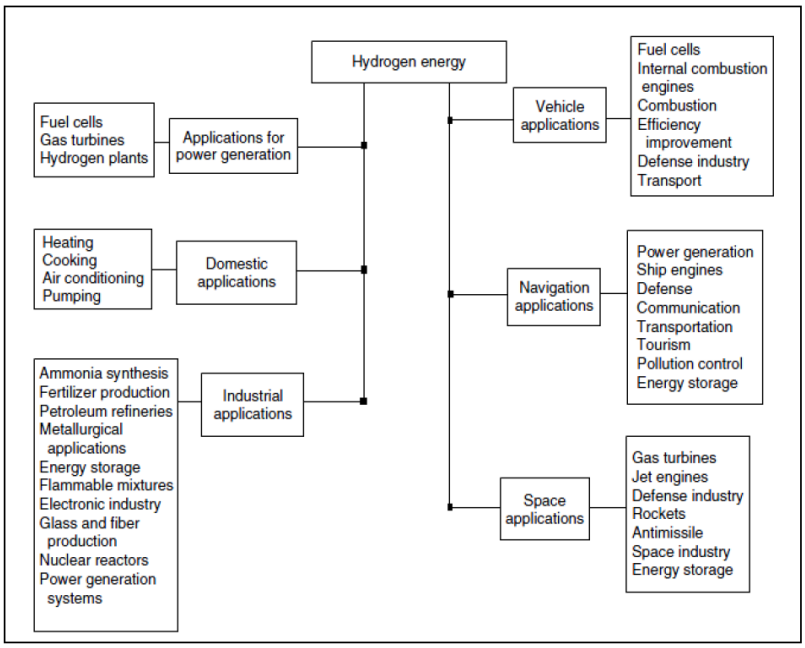

Figure I-4 Possible Hydrogen applications.

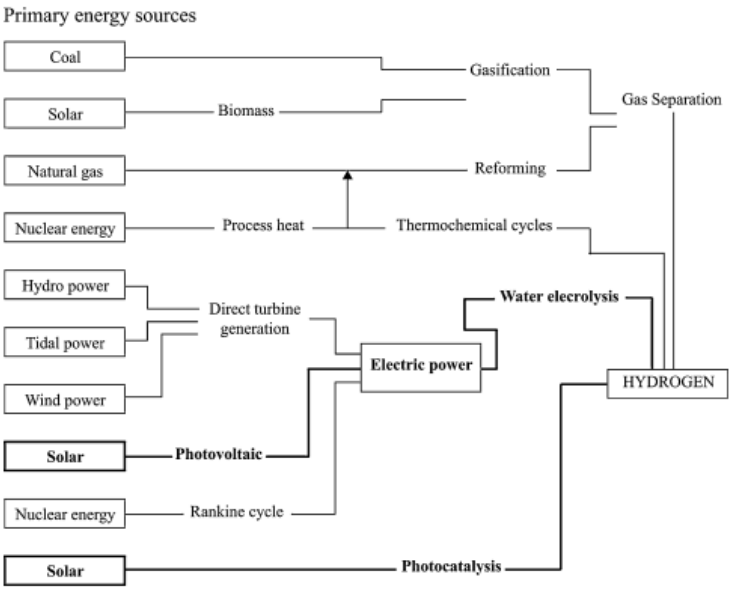

Figure I-5 Various methods for hydrogen generation.

1.3.1 Solar-driven hydrogen production via photoelectrochemical water splitting

Renewables are used for sustainable production of hydrogen. Solar energy has been always the main and primary source of energy on earth. To this end, the solar energy reaches earth daily is about 200,000 times the world's generating capacity of electricity per day [22]. Thus, solar energy is the most promising and reliable source of energy for sustainable production of hydrogen and towards hydrogen-driven economy. As shown in **Figure I-5**, there are two solar-based approaches for hydrogen production namely; the photovoltaic water electrolysis and the direct water photolysis. In former method, there is a need for an integrated system while the latter consist of a cheaper stand-alone system. In this regard, the scope of this study encompasses the direct water photolysis (herein referred to as photoelectrochemical (PEC) water splitting) is the adopted technique in this study that will be discussed further in chapter II. Since the first demonstration of Solar-driven water splitting in 1972 [23], the scientific community is striving to design an efficient, durable, reliable, stable, and robust semiconductor-based photoelectrochemical (PEC) system in quest of the maximum theoretical solar-to-hydrogen (STH) efficiency of 29.7% [24]. Given that the maximum practically achieved STH efficiency is still lagging below 1.0% [24], an immense demand of persistent efforts for revolutionizing the performance of the PEC main components is needed. A typical PEC system consists of photoelectrodes, electrolyte, and a separation membrane [25]. In PEC system, the adequate performance relies heavily on the photoelectrodes. Therefore, optimizing the properties of the photoelectrodes is of paramount significance towards the advancement and the commercialization of feasible cost-effective PEC systems for water splitting [24].

1.3.1.1 Tuning Metal Oxides for Water Splitting applications

The key factors that dictate the quality of a photoelectrode are the energy band-gap, electron-hole recombination, stability, and the photocurrent density[24]. Metal oxides possess high photoelectrochemical stability, wide range of bandgaps and satisfactory band edge

positions [26], yet they have limited light absorption, high recombination rates, poor electrical conductivity, and short hole diffusion length [24]. Defect engineering through doping is identified as an effective approach to enhance the optical and electronic properties of metal oxides. Doping improves the light absorption of the material by introducing defect states that narrow the bandgap and improves the conductivity [27].

1.3.1.2 Carbon defects and Zirconia within the Water Splitting context

A myriad of dopants and defects in metal oxides were explored for water splitting applications [6–15]. Among the various dopants, carbon doping in titania raised a huge controversy in literature whether it can induce visible light absorption or not. Nevertheless, numerous experimental and computational studies showed promising results of specific carbon defects in titania for water splitting applications [38–44]. Similar to titania, zirconia is a wide-gap metal oxide with distinctive properties such as high melting-point, chemical inertness and high corrosion tolerance [45] that render it advantageous for a plethora of applications [28-49]. However, the bandgap of zirconia needs to be optimized to enhance its photocatalytic activity. Unlike titania, the use of zirconia in water splitting systems has been poorly addressed in literature. A few studies shed the light on the effect of various dopants on the performance of zirconia in solar-driven hydrogen production systems.[68–70]

1.4 Supercapacitors for energy storage

Generated energy should be available for usage over the course of time and place. Thereby, energy storage is of equal importance to energy conversion. Since solar energy is the main source of the upcoming energy technology. Research has focused on developing energy storage devices for integration with the solar energy conversion devices to allow the best performance of the overall system. Solar cells and solar panels have been integrated with

different batteries and supercapacitor devices [71,72]. However, since supercapacitors can provide a faster charging (higher power density) and long living cycling stability, it has been the next generation of the energy storage devices [73]. On the other hand, supercapacitors lack the high energy density generated in batteries. Therefore, research have been intense on developing high energy density supercapacitor electrodes [74]. To this end, supercapacitors can store energy using three different mechanisms as presented in **Figure I-6** [7].

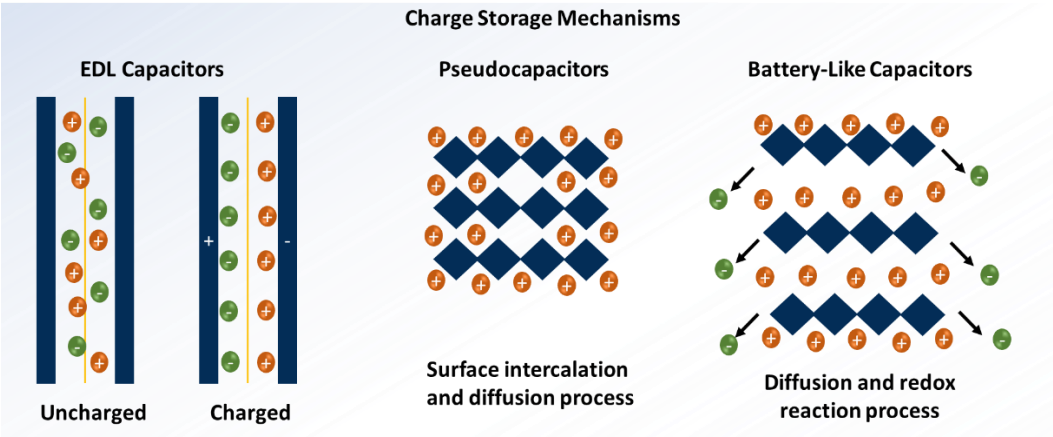

Figure I-6 Supercapacitor charge storage mechanisms.

The first mechanism is by using a simple adsorption/desorption on the surface of the electrode material named electrical double layer (EDL) capacitance [75]. The EDL capacitance usually exists in the carbon electrodes and is limited with the surface area of the electrode material. However, EDL capacitors can provide a very high cycling stability [76]. The second mechanism is the pseudocapacitance in which the electrode material can undergo surface EDL capacitance along with surface redox reaction or surface intercalation [75]. The pseudocapacitance can provide higher capacitance values, however, it can decompose and/or corrode upon increasing voltage and over high cycling number. For the third mechanism, it is the battery-like capacitor in which the electrode material can undergo a redox reaction and act as a battery [75]. The battery-like capacitors can provide a very high capacitance value, but its potential window is very low [74]. Besides, pseudocapacitors and battery-like capacitors are electrolyte dependent that they only undergo their reactions in specific pH and with specific ionic systems [77].

1.4.1 Carbon-based Supercapacitors

For adjusting both the capacitance values and the stability, research have pointed towards the use of hybrid electrodes of both carbon materials and other faradic materials (materials that can undergo redox or intercalation reactions) [76,78]. Therefore, the investigation of the properties of the carbon materials to be used in electrodes can give insights on the development of the supercapacitor performance. Since carbon electrodes depend basically on the EDL capacitance, their surface area is of great importance. Researchers have targeted the increase of the surface area through using 2D materials such as graphene and graphene-doped electrodes or developing porous carbon materials [79]. However, the surface area is not the only controlling parameter in the capacitance performance of the carbon material. Since the synthesis of new carbon materials can cost a lot of funds, effort and time, a screening method should be used to investigate the properties of the carbon materials prior to the synthesis step. Density functional method (DFT) have proven to be a good alternative to the guess and check method. Supercapacitor carbon electrodes can be investigated using either the classical DFT (cDFT) or the electronic DFT (eDFT) [7]. cDFT usually gives insights on the morphology and porous structure of the carbon material, while the eDFT gives insights on the electronic system of the carbon material [7]. Carbon materials can undergo different quantum behaviour upon applying voltage depending on their electronic states. This quantum behaviour (referred to as quantum capacitance (QC)) can affect the capacitance performance of the electrode material dramatically. The quantum capacitance can be calculated effectively using DFT tools represented in density of states (DOS) [7].

1.5 Scope of thesis

Although carbon-doped zirconia was briefly investigated in the literature [80–82] the debateable effect of carbon doping in zirconia was neither treated nor unriddled systematically and comprehensively for water splitting applications. The first-principles calculations proved

to be credible and efficient in diverse applications [4–10]. Therefore, Herein, an in-depth first-principles study was conducted to encompass the viable scenarios for doping monoclinic zirconia with carbon and to scrutinize the effect of carbon doping on its performance metrics as a photoelectrode for water splitting. Particularly, this study investigated the thermodynamic, electronic, and optical properties of the studied defects to report the best candidate defective structure for the photoelectrodes of PEC systems. The study also aims at using DFT in predicting the capacitance performance of carbon electrodes in supercapacitors through employing the quantum capacitance as a performance indicator for investigating the effect of structural variation and N-doping in various carbon materials.

Chapter II : Background

2.1 Density functional theory principles

In this study, density functional theory (DFT) was used as the main tool for investigation of the properties of the studied materials. In this chapter, the origin and principles of the DFT will be explained in detail.

2.1.1 Quantum mechanics

One of the key properties that can give fundamental insights on all other static properties is the total energy of the system. It can also predict the changes in the system over the course of time. However, the accuracy of the theoretically calculated properties depends directly on the accuracy of the calculated total energy. The total energy for a system consisting of a number of particles, can be calculated as the summation of the potential energy of the individual particles and their kinetic energies [83–85]. The potential energy term usually results in complications due to the interactions between particles of the system. For quantum mechanical systems (eg. electrons), the potential energy term can even become more complicated. In these regards, the quantum mechanical wave equations can be used to describe the potential and kinetic energies of those small particles taking into consideration the system dynamics.

For this reason, quantum mechanics was taken as the most extensive scientific development in the twentieth century [86]. It was confirmed by experimental observations that this theory can accurately describe the materials and their properties. For non-relativistic systems, solving Schrödinger equation can give the ground state energy. To this end, Schrödinger equation can solve exactly the systems of one or two particles and hence, the ground state and their relative properties can be accurately calculated. However, for systems with a larger number of particles, the energy cannot be solved exactly, and approximations should be employed.

2.1.2 Hamiltonian operator

The information of the system can be obtained along with the fundamental interactions between particles in the system and can be defined by a mathematical operator named "Hamiltonian (Ĥ)". If the Ĥ was defined, all the properties of the system can be identified (both the chemical and physical properties). This study deals with nanomaterials that is represented by a system containing atoms and electrons in the micro scale and is governed by quantum mechanical laws. Therefore, the physical and chemical properties of our systems should be defined by solving the Schrödinger equation. Accordingly, it is needed to choose the most accurate approximation for solving the Schrödinger equation and hence the Ĥ. One of the most used approximations is the Born-Oppenheimer approximation in which the electronic and nuclear motion is decoupled.

2.1.3 Schrödinger equation calculation

The electrostatic interaction term is the most important part of Schrödinger equation for solid state chemistry calculations. Relativistic effects can be neglected, if considering the valence electrons only. To simply describe the Ĥ, a preliminary step can be considered in terms of neglecting the spin effect of electrons in both valence and core of the system. The non-relativistic time independent Schrödinger equation can describe a system with defined valence electrons and nuclei in which the Ĥ consists of 5 terms, three of them are the potential energy terms while the other two are related to the kinetic energy terms:

$$H= T_n + T_e + V_{n-n} + V_{n-e} + V_{e-e} \quad \text{(II-1)}$$

The four terms can be calculated according to the following equations, with neglecting the spin property:

$$T_n = \sum_{I=1}^{L} \frac{P_I^2}{2M_I} \quad \text{(II-2)}$$

$$T_e = \sum_{i=1}^{N} \frac{P_i^2}{2m} \quad \text{(II-3)}$$

$$V_{n-n} = 0.5 \sum_{I \neq J}^{N} \frac{Z_I Z_J e^2}{|R_I - R_J|} \quad \text{(II-4)}$$

$$V_{n-e} = -\sum_{I,J} \frac{Z_I e^2}{|r_i - R_I|} \quad \text{(II-5)}$$

$$V_{e-e} = 0.5 \sum_{I \neq J} \frac{e^2}{|r_I - r_J|} \quad \text{(II-6)}$$

Z_I refers to the charge of the I^{th} electrons. The 0.5 factor was used in both Vn-n and Ve-e to cancel the double counting of interaction between the same pair of particles. By identifying those 4 terms, the Schrödinger equation can be theoretically calculated, and the energy of the system can be defined using the $\hat{H}$:

$$H\Phi(R,r) = E\Phi(R,r) \quad \text{(II-7)}$$

However, the wavefunction symmetry is not included in the previous expression of the potential and kinetic energies. For fermions such as electrons, the quantum statistics must be inserted using Pauli Principle. When quantum statistics are considered properly in the system, this leads to the insertion of an energy term named the exchange-correlation term which affects a term called the effective Hamiltonian. Moreover, the relativistic effects can be neglected for lighter elements. However, for heavier elements, the wavefunction will be very localized for core electrons and the relativistic effects should be considered to suit the high kinetic energy resulted from the localization of the core electrons. The energy difference between the system energy with and without the presence of quantum statistics can derive these effective terms. However, solving Schrödinger equation is considered impossible in its direct way. On the other hand, approximations can be applied to allow a variety of accurate solutions to Schrödinger equation. The first step in the ladder of approximations is the Born-Oppenheimer approximation [87].

2.1.4 Born-Oppenheimer approximation

An electron is generally so small in the range of 1/2000 of the mass of the proton. However, for hydrogen and helium atoms, the mass of the kinetic energy of an electron can reach ~ 100 times larger than that of the nuclei [87]. For that reason, the it was suggested that the motion of the electron will follow that of the nuclei immediately and will be in their ground state along all the nuclei configuration. Then the potential of the electron movement is defined by the electronic state. Thus, the Born-Oppenheimer approximation is dealing with the separation of the processes time scale including the electrons and atoms. To this end, the $\hat{H}$ can be calculated as one kinetic energy term resulted from the nuclei. However, the nuclei are considered static with the electrons only moving in the atoms. Hence, the $\hat{H}$ can be named electronic Hamiltonian H_e with a fixed nucleus coordination $\{R\}$ and can be represented as following:

$$H_e(\{R\})\psi(r,\{R\}) = E_e(\{R\})\psi(r,\{R\}) \quad \text{(II-8)}$$

with $E_e(\{R\})$ is the Born-Oppenheimer energy surface.

Moreover, the motion of the nucleus can be treated using classical equations such that the quantum effects are ignored, and the equation is solved for the nuclei motion only in the so-called atomic Schrödinger equation. However, the accuracy of the Born-Oppenheimer approximation cannot be proved since it ignores the electronic transitions resulted from the nuclear motion, hence the description of the processes containing electronic transitions is hard to be calculated. Yet, the Born-Oppenheimer approximation still can be successful for prediction of properties of nanomaterials [87].

2.1.5 Progress of DFT

One of the widely used computational tools is the density functional theory (DFT) since it is relatively non-expensive with acceptable accuracy for computing electronic properties for

the many-body systems [88–91]. DFT treats the many-body system using the electronic charge density instead of the wavefunction normally used with Schrödinger equation to get the fundamental variables [88,89,91,92]. The accuracy of this method originates from the fact that each material has its particular electronic structure and hence its particular electronic density.

Quantum mechanics tries to give the total energy through solving Schrödinger equation which requires solving the many-body function that cannot be observed directly. However, the probability of finding N electrons at a particular place (r1, . . . , rN) can be measured theoretically and it can be defined as $\Psi^*(r1, \ldots, rN)\Psi(r1, \ldots, rN)$. Noteworthy to say that all the electrons in a system are identical, hence electron 1 is the same as electron 2 and the calculations are not restricted by the numbering of the electrons and the probability of finding N electrons can be identified using any order. To this end, the density of electrons at a coordinate of space n(r) is directly related to the probability of finding the N electrons. And the electronic density can be identified as the summation of the wavefunctions of each electron. Thus, the electronic density is defined as the summation of the probability that a specific electron with a specific wavefunction exists at a position r and the equation can be written as following:

$$n(r) = 2 \Sigma \psi_i^*(r)\psi_i(r) \qquad \text{(II-9)}$$

The factor of 2 in the previous equation resulted from the application of Pauli principle stating that two electrons with the same spin cannot occupy the wavefunction. To this end, the electronic density n(r) can give a lot of information about the system since it is a function of 3 coordinates that can be solved to result in an accurate wavefunction solution for the Schrödinger equation.

2.1.5.1 Hohenberg-Kohn theorem

Hohenberg-Kohn identified the DFT using two fundamental theorems. The first DFT theory states that ***"The ground-state energy from Schrödinger's equation is a unique functional of the electron density."*** [86]

That theory identifies the unique ground-state wavefunction using the unique ground-state electronic density. Hohenberg and Kohn used mathematics tools to describe the ground-state energy E as a function of electronic density n(r), E[n(r)]. Hence, E is a function of n(r) and n(r) is a function of another function which is where the word "Functional" in "Density Functional Theory" came from. Therefore, the properties of any material can be predicted using its unique ground-state wavefunction and electronic density. To this end, the properties of a material can be calculated by solving the electronic density functional of the three coordinates instead of solving the wavefunction of the 3N variables. In this regard, a nanomaterial of 100 Cu atoms with thousands of dimensions, the electronic density functional can be solved using only three dimensions. Although the Hohenberg-Kohn theory presented a successful model to find an accurate energy representation for the system using electronic density instead of the wavefunction, it did not identify the exact functional to be used. For that reason, a second theorem was modified to give the set of the wavefunctions n(r) corresponding to the ground-state electronic density. The theory states that **"*The electron density that minimizes the energy of the overall functional is the true electron density corresponding to the full solution of the Schrödinger equation.*"** [86]

In this second theorem, the functional is being solved using variety of densities until it reaches a minimum value which refers to the ground-state electronic density. Thus, the ground-state energy can be written in the form of $\Psi_i(r)$ [single electron wave functions] that are collected to define the n(r). Finally, a functional is formed from two terms (a known and an unknown).

$$E[\{\psi_i\}] = E_{known}[\{\psi_i\}] + E_{XC}[\{\psi_i\}] \quad \text{(II-10)}$$

$$E_{known}[\{\psi_i\}] = \frac{h^2}{m}\sum_i \int \psi_i^* \nabla^2 \psi_i d^3r + \int V(r)n(r)d^3r + \frac{e^2}{2}\iint \frac{n(r)n(r')}{|r-r'|} d^3r d^3r' + E_{ion} \quad \text{(II-11)}$$

The E_{known} is represented by 4 terms, the first is the electronic kinetic energies, the second is the electron-nuclear Coulomb interactions, the third is the electron-electron interactions, and the fourth is the nuclear-nuclear interactions.

The wavefunction's second term is the exchange correlation function ($E_{XC}[\{\Psi_i\}]$), it contains all the effects resulted from quantum mechanics that the known term did not include them. Moreover, Kohn and Sham (KS) proved that solving some equations with only one electron in each equation can pave the way to find the right electronic density.

$$[\frac{h^2}{2m}\nabla^2 + V(r) + V_H(r) + V_{XC}(r)]\ \psi_i(r) = \varepsilon_i\ \psi_i(r) \quad \text{(II-12)}$$

$$V_H(r) = e^2 \int \frac{n(r')}{|r-r'|} d^3r \quad \text{(II-13)}$$

where V(r) is the electron-nuclear interaction energy term, which is one of the known energy functionals, $V_H(r)$ represents the Hartree potential term, V_{XC} is the exchange-correlation functional. All the three V(r), $V_H(r)$, and V_{XC} represent the potential energy term. The previous equation can define the position vector (r) using only 3 variables. $V_H(r)$ can identify the interaction between the total density of the electrons in the system and a considered electron in the system. This interaction can be classified as a self-interaction including the electron interacting with itself. That self-interaction should be corrected which can be described by the V_{XC} term.

It is important for solving the Kohn and Sham equation to find the ground-state electronic density and hence the V_H term. However, to get the V_H term, it is required to find the single electron wavefunction through solving Kohn and Sham equation. This puzzle can be overcome through some calculations. First, the electronic density n(r) should be assumed using an initial guess. Then, the V_H can be calculated in terms of the suggested n(r). After that, the Kohn and Sham equation can be solved to get the single electron wavefunction $\Psi_i(r)$. Then, that

$\Psi_i(r)$ can be used to find the new n(r). Finally, the new calculated n(r) should be used to calculate V_H and the steps are repeated until the initial n(r) is equal to the calculated n(r). However, this algorithm missed the point of how to make a first guess for the initial electronic density.

2.1.5.2 The Exchange-Correlation Functional

One of the active research points in DFT science is to develop a functional that can describe the exact nature of the exchange-correlation (XC) functional. To this end, there is only one special case in which the XC functional is well known, which is the uniform electron gas. For a uniform electron gas, the n(r) is constant in all coordinates. However, in a real material, the electronic density varies over the space and directions. On the other hand, the case of the uniform electronic gas can be used to give insights on the practical use of the Kohn and Sham equation. In this practical application, a known exchange-correlation potential can be defined at each position in the system using the electronic density observed from the uniform electron gas at this position.

$$V_{XC}(r) = V_{XC}^{elec.gas}[n(r)] \qquad \text{(II-14)}$$

Furthermore, this approximation uses the local density only to approximate the exchange-correlation function namely Local Density Approximation (LDA). However, this LDA pathway cannot identify the true structure of the exchange-correlation functional. Although the theoreticians did not find "yet" an accurate mathematical solution that can be used for all systems, there are many formulae that can give accurate acceptable results. Therefore, it is important to know which XC functional to use when dealing with a particular system. As an example, one of the most widely used functionals is the Generalized Gradient Approximation (GGA) which combines both the LDA information and the local gradient of the electron density. However, the GGA is not always accurate or suitable for all systems and sometimes LDA can give more accurate results. On the other hand, the GGA itself contains a high number

of functional since the local gradient of the electron density can be identified using different routes and mathematical formulae. The wavefunctions should satisfy the real electronic properties for a system of N-electrons in N-directions to allow an accurate mathematical solution for the quantum mechanical properties of the system and hence for the approximations applied on the wavefunction resulted.

2.1.6 DFT proposed corrections for the electronic properties problem

To give an accurate prediction for the properties of the modelled material, it is important to describe the electronic structure correctly. However, there is a famous bandgap problem in the semiconductor correlated materials. On the other hand, many approaches were adopted by researchers to address this problem and provide accurate solutions. One of the cheapest approaches computationally is the Hubbard correction (DFT+U) approach. The Hubbard correction can provide an accurate prediction for the electronic properties of highly correlated materials. However, the optimization of the U value (Coulomb interaction potential) needs more semi-empirical methods to be achieved.

2.1.6.1 Proposed corrections and their accuracy

DFT can provide a structural and cohesive properties accurately. However, it cannot predict the electronic related properties with the same accuracy for semiconductor materials [93]. Therefore, computationally expensive tools such as hybrid functionals that solves the Hartree-Fock (HF) equations exactly or larger basis sets should be employed to give more accurate results [86]. Reaching a more accurate electronic structure is crucial for predicting the needed properties such as the bandgap and the formation energy. Noteworthy to mention that hybrid functionals can fail to give accurate electronic properties with semiconductors with strong electron correlation (Mott insulators) [94,95]. Alternatives to hybrid functionals have been developed to save time and to give more accurate results. One of the major alternatives

employed is the DFT+U (Hubbard correction) which can give accurate results for electronic properties such as the bandgap. One of the major advantages of DFT+U besides its accurate results, is its low computational cost. The correct electronic structure calculated from the DFT+U can then be used to give more information about the system such as the formation energy and the intermolecular interactions [95]. Moreover, the DFT+U can provide accurate results for the physical properties as well such as the magnetic properties and the structural properties for the highly correlated systems. However, the major disadvantage of the DFT+U is its failure to predict properties of material with delocalized electrons (e.g. metals). The key point for the successful results of the Hubbard correction is its simple approach for getting over the underestimated interactions between electrons through adding a numerical value (U) using semi-empirical method [94]. This method makes the Hubbard correction a good tool to give insights on the effect of the electronic correlation on the physical parameters of the system. To this end, the Hubbard correction can be used along with most of the DFT functionals such as the LDA+U, and the GGA+U.

2.1.6.2 Highly correlated systems problem

The sum of the Hartree term ,which represents the Columbic repulsion between the density of the electrons, and the exchange-correlation term (XC) ,which represents the spin interaction and all the correlation, can describe the interaction energy [89]. However the accuracy of the DFT calculations depends mainly on the accuracy of the approximations used to calculate the exchange-correlation term [90]. Generally, the XC functional cannot represent the many-body properties for an N-electron system accurately since the dependence of the XC functional on the electronic density is difficult to be modelled. Therefore, highly correlated systems which are the systems that have its physical properties controlled by interactions between the many-body electrons cannot be accurately described using the direct DFT approaches. This problem results in some electronic modelling difficulties such as the bandgap modelling problem reflected in poor prediction of the transition states and intermolecular interactions [96].

The problem with using DFT to describe the highly correlated systems resulted from the XC functional representation of those systems represented in over estimation of the delocalization of the valence electrons and the stabilization of the ground state of the metallic nature [94,95]. For that reason, DFT usually fails to predict the properties of the highly correlated systems which include a ground state with more localized electrons. The over-delocalization resulted from the XC functional can be attributed to the inability of the functional to remove the self-interacted electrons contained in the Hartree term which in turn gives a remaining term representing the self-interacting electron which adds a delocalization for the wavefunction [95]. One of the solutions to this problem is the hybrid functionals that contain a Hartree-Fock exchange functional and a linear combination of exchange-correlation density. Those terms are considered self-interaction-free since the self-interaction of the electrons is eliminated through the presentation of the Fock-exchange term. However, the hybrid methods are computationally expensive and cannot be used easily for large systems or complex systems. Moreover, the Hartree-Fock method fails to describe the physical properties of the highly correlated systems since it describes the electronic structure using only an optimized determinant. For describing the highly correlated systems, a full multi-determinant for the N-electron wavefunction should be taken into consideration besides the many-body terms [94]. To this end, it can be concluded that using DFT approximations such as the LDA and GGA cannot describe the physical properties of the highly correlated systems.

2.1.6.3 The Mott insulators

Mott insulators are materials that give both metallic and insulating properties when measured using different tools. Those materials give a metallic nature when modelled using the band theories while they show an insulating behaviour when measured experimentally. Nevil Mott pointed out this behaviour in the band theory which indicate that the interelectron forces can lead to the presence of a bandgap instead of modelling the material as conductors [97]. In those Mott insulators, the bandgap is generated due to the presence of Hund's rule of the crystal

field splitting between the sub orbitals of the same orbital (e.g. 3d orbital). This insulating behaviour results from the Coulomb repulsion generated between the electrons in the same orbital enforcing them to localize in their orbitals. A "U" value was suggested by Hubbard to represent this strong Coulombic potential that arises among the highly-correlated electrons. Moreover, the localization of electrons results in a restriction in the movement of the electrons enforcing them to jump between atoms "hopping mechanism", this jump has an amplitude of a transfer integer (t) which is proportional to the bandwidth of the valence electronic state. Therefore, the bandgap can be formed with a competition between (t) and (U). And the energy of the bandgap can be calculated using the following equation where (z) is a term representing the number of the neighbouring atoms [95].

$$E_{gap} = U - 2zt \quad \text{(II-15)}$$

Hence, the Hubbard Hamiltonian can be formulated in a simpler method such as [95]:

$$\text{Hub} = t \sum_{(i,j),\sigma} \left(c^*_{i,\sigma} c_{i,\sigma} + hc \right) + U \sum_i n_{i\uparrow} n_{i\downarrow} \quad \text{(II-16)}$$

where (i,j) represents the nearest neighbour atomic sites, C* is the electronic creation, C is the annihilation, and n is the number of operators for electrons of a specific spin in site i. It can be noted that (t) is proportional to the dispersion of the valence electrons, on the other hand, (U) is proportional to the atomic state occupation numbers on the same site. The bandgap results from the insufficient energy of the electrons that hinders them from overcoming the repulsion potential of electrons in the neighbouring sites ($t < U$). However, when $U > t$, DFT can accurately predict the electronic properties.

2.1.7 The Hubbard Correction

The Hubbard correction namely DFT+U has a main advantage of being easy to be added to the DFT methods without a significant computational cost. The U correction can be implemented in both the LDA approximations and the GGA approximations. The Hubbard

Hamiltonian treats all the valence electrons using the normal DFT methods except for the highly correlated d and f orbitals. The U correction can be added to the DFT functional after identifying the on-site interaction strength. The U term "Coulomb potential" and a J term "site exchange" can identify the on-site interaction and they can be calculated through ab-initio methods or semi-empirical methods. In order to add the U correction to the DFT functional and provide an accurate solution, the approximation itself should be well understood and the conditions of the system should be considered [94,95]. For the LDA functional, the total energy E_{LDA+U} can be calculated as the summation of the Hubbard functional (for correlated states) and the LDA energy functional (for all states). It should be noted that adding this Hubbard term will cause a double counting for the correlated states. Therefore, a new term E_{dc} should be removed from the calculated total energy [94].

$$E_{LDA} + U[\rho(r)] = E_{LDA}[\rho(r)] + E_{Hub}[\{n_{mm}^{I\sigma}\}] - E_{dc}[n^{I\sigma}] \quad \text{(II-17)}$$

To this end, the U correction can be considered as the substitution of the electronic interaction of the mean field in the exchange-correlation functional. Moreover, the E_{dc} is not unique for each system and can be defined for many systems at the same time. One of those formulations is the fully localized limit (FLL) which can be applied on more localized electrons on an orbital system [98,99]. This formulation is commonly used since it can expand the width of the orbitals of Kohn and Sham while considering the Mott localization. This formula identifies the LDA+U as following:

$$E_{LDA+U}[\rho(r)] = \sum_l [\frac{U^l}{2} \sum_{m,\sigma \neq m',\sigma'} n_m^{l\sigma} n_{m'}^{l\sigma'} - \frac{U^l}{2} n^l (n^l - 1)] \quad \text{(II-18)}$$

where $n_m^{I\sigma}$ is the occupation number of the localized orbitals in which I is the site index, m is the state index, and σ is the spin. It is expected that the U correction will depend on the occupation number since it depends on the states which are affected by the correlation effect and are the most distributed. Therefore, assisting the electronic Mott localization on specific states will lead to reduction in the fractional occupation of the localized orbitals [94].

The rotation of the basis set of the atomic orbital that defines the occupation number is not well modelled in the Mott localization model. Therefore, a rotationally invariant formulation should be used (unitary-transformation-invariant) along with the LDA+U [98]. This formulation can be considered the most complete one for the LDA+U since the electronic interaction depends fully on the orbitals. A simplified form of U is the U_{eff} which is an effective U parameter equals U-J where J is the exchange interaction resulted from Hund's coupling rule. To this end, the U_{eff} is preferred since the J parameter is important for many systems especially those with spin-orbit coupling.

2.1.8 Perdew–Burke-Ernzerhof (PBE) approximation

In KS equation, the E_{XC} should be approximated as a function of spin densities in order to find an accurate result. One of those approximations is the local spin density approximation (LSD) which only vary the densities slowly to reach the appropriate results using the following equation where n is the summation of $n_{\uparrow}$ and $n_{\downarrow}$ [100]:

$$E_{XC}^{LSD}[n_{\uparrow}, n_{\downarrow}] = \int d^3rn \in_{XC}^{unif} (n_{\uparrow}, n_{\downarrow}) \quad \text{(II-19)}$$

Another important approximation is the generalized gradient approximation (GGA) which can improve the electronic results namely, the atomization energy, the total energy, and the energy barriers. This improvement may be attributed to the ability of the GGA to expand and soften the bonds and it can deal with the inhomogeneous density which makes it correct the LSD results [100]. the GGA can identify the total energy as following:

$$E_{XC}^{GGA}[n_{\uparrow}, n_{\downarrow}] = \int d^3rf(n_{\uparrow}, n_{\downarrow}, \nabla n_{\uparrow}, \nabla n_{\downarrow}) \quad \text{(II-20)}$$

Choosing the right $f(n_{\uparrow}, n_{\downarrow}, \nabla n_{\uparrow}, \nabla n_{\downarrow})$ still a tricky mission, it can be estimated using either a semi-empirical methods or ab-initio methods. However, the semi-empirical methods fail for metals and gases. On the other hand, the ab-initio methods can provide a better solution since it starts from the exchange correlation hole second order density gradient expansion of

the electron and slowly vary the density, after that, the long range parts are cut off to follow the sum rules [100]. In 1996, Perdew, Burke, and Ernzerhof suggested a modification for the GGA approximation and developed the PBE energy as following [100]:

$$E_{XC}^{PBE}[n_{\uparrow}, n_{\downarrow}] = \int d^3rn \in_{XC}^{unif} (n)\, F_{XC}(r_s, \zeta, s) \qquad \text{(II-21)}$$

where ζ is the spin polarization and equals $(\rho_{\uparrow}- \rho_{\downarrow})/\rho$, r_s is the Wigner–Seitz radius and equals $(4\Pi\rho/3)^{(-1/3)}$. It was proved that the E_{XC}^{PBE} increases with increasing the electronic density because of the deeper exchange-correlation hole that makes it more localized [101]. To this end, the PBE method was proved to have an acceptable accuracy and low computational cost over other DFT methods. Therefore, in this study, the PBE will be adopted to give the most accurate and acceptable results.

2.1.9 Van der Waals implementations in DFT

Layered structures can develop a London force between layers namely the Van der Waals forces (VdW), those forces have a great impact on the resulted total energy and must be taken into consideration when calculating the DFT energy term. However, dispersion functionals can be applied to the DFT functionals to overcome this effect [102]. Grimme et. al have developed a dispersion functional named DFT-D3 to account for the VdW forces and to be applied as a DFT approximation as following [102]:

$$E_{disp}^{DFT-D3} = -0.5 \sum_{A\neq B} \sum_{n=6,8} s_n \frac{C_n^{AB}}{R_{AB}^n} f_{damp,n}(R_{AB}) \qquad \text{(II-22)}$$

$$f_{damp,n}(R_{AB}) = \frac{1}{1+e^{-\gamma\left(\frac{R_{AB}}{s_{r,n}R_0^{AB}}-1\right)}} \qquad \text{(II-23)}$$

where, the summation is for all the atomic pairs in the system, R_{AB} is the internuclear distance, C_n^{AB} is average n^{th} order dispersion coefficient for the atoms A and B, s_n is the global DF dependent scaling factor (usually s_6 is the commonly used value and is set to unity in DFT-D3 to correct the long range behaviour), $f_{damp,n}$ is a damping function to overcome the double

counting in the functional and can be used to give the dispersion correction range, R_0^{AB} is the cut-off radius of the atomic pair computed non-empirically, γ is a constant that is used to give the steepness of the functions.

Another approximation that requires a lower computational cost and can give a similar accurate result is the DFT-DF2 approximation.

$$E_{XC}^{VdW-DF2} = E_X^{rPW86} + E_c^{PWLDA} + E_{c-nl}^{VdW-DF2} \quad \text{(II-24)}$$

$$E_{c-nl}^{VdW-DF2} = 0.5 \iint dr dr' \rho(r)\rho(r')\emptyset(r,r') \quad \text{(II-25)}$$

where E_X^{rPW86} is the exchange functional of the refitted PW86 functional, E_c^{PWLDA} is the local correlation part of the PW86 functional, and $E_{c-nl}^{VdW-DF2}$ is a term added to the converged functional PW86 and the functionals (rPW86 and PWLDA) vary in the definition of the kornel ∅(r,r') [102]. This DFT-DF2 functional has proved to give accurate results for carbon materials with VdW forces that are used in this study [102–104].

2.2 Applications

2.2.1 Photoelectrochemical water splitting

Splitting or dissociation of water into its elemental species (H_2 and O_2 molecules) is an uphill reaction in terms of energy where this reaction requires 1.23 eV per electron or ΔG^0 (standard free energy change) of 237.2 kJ/mol as shown in **Figure II-1** [19]. For undergoing water splitting, two H^+ ions need two electrons to produce a single H_2 molecule (reduction of H ions or proton reduction) while four holes are required to produce a single O_2 molecule (oxidation of O ions or water oxidation) as indicated in the equations below.

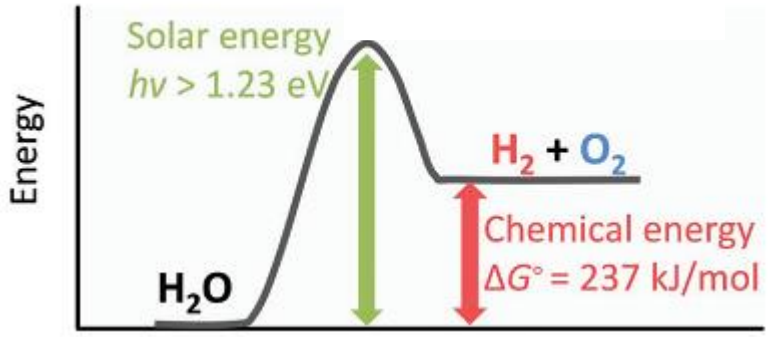

Figure II-1 The energetics of water splitting uphill reaction.

Oxygen Evolution Reaction (OER): $2H_2O + 4h_{vb}^+ \rightarrow O_2 + 4H^+$ (II-26)

Hydrogen Evolution Reaction (HER): $2H + 2e_{cb}^- \rightarrow H_2$ (II-27)

One of the possible ways to get the necessary energy to drive the water splitting redox reaction, is to absorb it from the solar energy spectrum via semiconductor (SC) which in turn produces photogenerated charge carriers (electrons (e_{cb}^-) in the conduction band (CB) and holes (h_{vb}^+) in the valence band (VB)). It is important to mention that the bandgap (E_g) of the semiconductor (light absorber) has to be 1.23 eV at least (corresponding to photons of $\lambda < 1010$ nm) and the photon must possess energies greater than or equal the bandgap of the semiconductor to be absorbed; to supply the energy required for the reaction to occur as expressed below.

Light absorption via SC and photogeneration of charge carriers:

$$SC + h\upsilon \left(\geq E_g\right) \rightarrow e_{cb}^- + h_{vb}^+ \quad \text{(II-28)}$$

In addition to the bandgap requirement for the SC photoelectrode, the band edges (VB and CB) must straddle the redox potentials of the water species as shown in **Figure II-2** [19]. Thus, H_2/H^+ and O_2/H_2O lines must be bracketed between the E_{CBM} and E_{VBM} (conduction band minimum and valence band maximum energies) of the SC photoelectrode. For practical overall water splitting, the photoelectrodes the bandgap energy must be in the range of 1.6-2.4 eV to account for the kinetic overpotentials [19]. In a typical photoelectrochemical (PEC) water splitting cell, an n-type semiconductor is employed as a photoanode while a p-type semiconductor is employed as a photocathode.

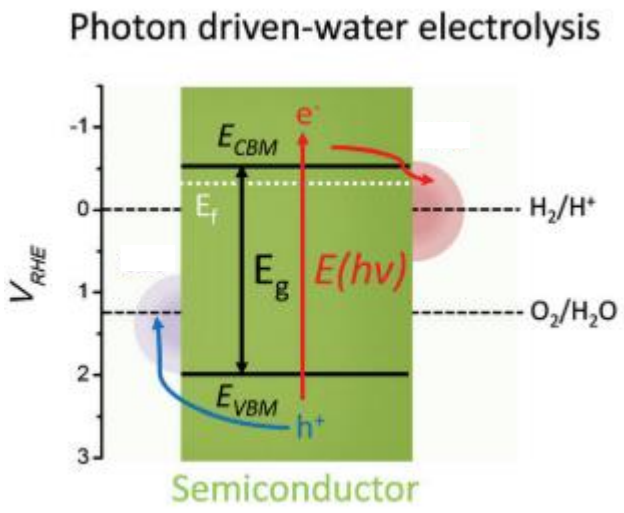

Figure II-2 Redox potentials for water species relative to the band positions of the semiconductor with respect to reference hydrogen electrode (RHE).

So in general, the criteria needed for a successful photoanodes are (i) the bandgap must be greater than 1.23 eV (theoretically) and 2 eV (practically), (ii) the redox potentials must be straddled by the band edge positions of the SC, (iii) the mobility and the lifetime of the electron-hole pair must allow the charge carriers to reach the active sites, (iv) the rate of OER should be higher than the competing recombination reactions, (v) the SC is required to be stable under illuminating and aqueous conditions [105].

2.2.2.1 Photoelectrochemical water splitting mechanism

Solar-driven water splitting systems can be categorized into (1) photoelectrochemical (PEC), (2) photocatalytic (PC), and (3) photovoltaic-electrochemical (PV-EC). The light will be shed here on PEC water splitting. The process of PEC water splitting as shown in **Figure II-3** [19] starts by (i) the light absorption of the photoelectrodes leading to the production of photogenerated electron-hole pairs (charge carriers) that induce photocurrents in photoanodes (n-type SC). (ii) The photo-generated holes oxidize the water at the photoanode. (iii) From the photoanode to the photocathode, the ionic transport of H^+ (hydrogen ions) occurs through the electrolyte while the electronic transport of electrons occurs via the external circuit. (iv) At the photocathode, the electrons reduce the hydrogen ions.

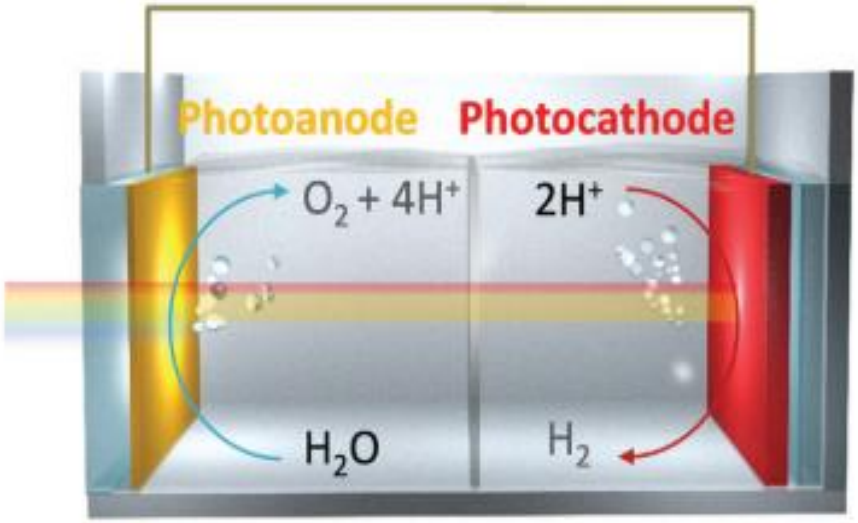

Figure II-3 Photoelectrochemical water splitting mechanism.

2.2.2.2 Tuning metal oxides to act as photoanodes

The selection and design of materials for the PEC system is very essential to obtain high performance. In this regard, the light absorber (photoanodes and photocathodes) is a key player that dictates the overall conversion efficiency. For practical photoanodes, it is very common to use n-type metal oxide SCs due to their stability in water. However, utilization of metal oxides in such endeavour face two main challenges. First, metal oxides have poor optical properties and wide bandgaps. Second, they have poor conductivity that is attributed to the low charge carrier mobility [19]. To improve the PEC performance of a given material class, there are several approaches. (i) Doping, (ii) development of heterojunctions, (iii) Co-catalyst loading, (iv) surface passivation, (v) nano-structuring [19]. Doping is the most common method to enhance the PEC efficiency for metal oxides through the introduction of intermediate defects states within the bandgap of the SC to reduce the bandgap. To narrow down the bandgap and to modify the bandstructure, dopants such as transition elements, N, S, and C are usually exploited to improve the light absorption, that leads to the improvement of PEC efficiency [106].

2.2.2 Quantum capacitance of carbon electrodes

In 1988, Luryi has presented the concept of quantum capacitance C_Q for semiconductors and is defined as the variation of electrical charge with respect to the variation of the electrochemical applied voltage (gate voltage) [107]. In solid state devices, the gate voltage can be used to vary the density of charge carriers (electrons or holes) through the field effect which in turn change the position of the Fermi level (E_F). For semiconductors, the position of the E_F represents the charge neutrality point that can be shifted from the valence band (V_B) to the conduction band (C_B) due to the change in the gate voltage [107]. For bulk semiconductors, the C_Q is misleading if it is compared to the real experimental values due to the fact that the insulator capacitance is much smaller than C_Q [108]. On the other hand, for 2D materials such as graphene and graphene-like structures, the DOS is highly affected by the E_F and hence, the C_Q can be affected greatly by the gate voltage [108]. Usually the 2D materials exhibit a minimum at the charge neutrality point when the conductance is measured as a function of the applied potential. This can be attributed to the fact that the DOS near the neutrality point is very small. For 2D materials with such a low DOS, the removal or addition of any electron can impact the electrode potential dramatically which gives a great importance to the calculation of the C_Q. Doping and using of variant carbon structures can enhance the intensity of the DOS near the neutrality point reflecting enhancement in the C_Q. In calculations of C_Q, the E_F is usually taken into account instead of the reference electrode and is considered as the potential of zero charge for the electrode (PZC) [7]. In summary, the C_Q has a greater impact in 2D materials than in bulk materials and is directly related to the DOS around the E_F.

Chapter III : Literature Review

3.1 The progress of DFT implementation for energy applications

In general, the design and the development of materials are very complicated, cost-ineffective, time-inefficient and resources consuming. The development of energy materials is not an exception. In the energy materials arena, there is a high demand and emphasis on the structural, thermodynamic, electronic, and optical properties. In this regard, first-principles calculations embodied in DFT pave the road for researchers to explore the aforementioned properties exploiting the quantum mechanics as the underpinnings for the modelling and simulation for the material at hand without any reliance on empirical parameters. By this way, DFT is instrumental in predicting the physical properties of novel materials. The pseudopotential-based DFT is the most widely used approach for the obtaining physical properties of energy materials [109]. For energy materials, the most common exchange-correlation functional (XC) adopted are the generalized gradient approximation (GGA) and local density approximation (LDA) [109]. However, GGA and LDA, typically, underestimate the energy bandgap of SCs and fail in describing the defect states. For energy materials, these shortcomings significantly affect the reliability of the results of such functionals. To mitigate these shortcomings, the research community resort to other approaches with higher computational cost. Among the approaches are; quasiparticle GW approximation, DFT+U, and hybrid functionals. DFT+U is the most convenient and computationally-efficient approach for strongly correlated electron systems or in other words; materials that contain d or f orbitals in their bandstructures. There are plethora of DFT calculations packages for materials simulations such as Cambridge Serial Total Energy Package (CASTEP), Vienna Ab initio Simulation Package (VASP), Quantum espresso, $DMol^3$ and Spanish Initiative for Electronic Simulations with Thousands of Atoms (SIESTA). In this study, CASTEP and VASP are utilized. CASTEP is a program based on quantum mechanics dedicated to serve solid-state physics and solid-state materials science. CASTEP adopts the plane-wave pseudopotential method to investigate

crystals and surfaces in various material classes. Furthermore, CASTEP can be used for defect studies [109]. VASP is a software implementation that models the electronic calculations and quantum mechanical molecular dynamics. VASP was developed based on the plane wave basis set. For the description of the electron-core interaction, VASP employs either Vanderbilt pseudopotentials or PAW method. Within VASP package, there are plenty of post-DFT corrections implemented like hybrid functionals, random phase approximations, HF exchange, and many-body perturbations. All of these implementations qualified VASP to be utilized in studying of thin-films, liquids, glasses, surfaces, interfaces, semiconductors, insulators, nanostructures, structure stability, phase stability, mechanical properties, optical properties, electrical properties, electronic properties, magnetic properties, and other applications [109]. Therefore, CASTEP and VASP are very convenient for energy materials studies.

3.2 DFT for PEC water splitting applications

DFT can be used to study different aspects and dimensions in PEC water splitting. In this part, the most important aspects would be covered.

3.2.1 Calculation of energy bandgap

For the improvement of wide-bandgap for SC, doping is a well-known technique to narrow the bandgap and enhance the optical properties for PEC water splitting. Asahi et al. attempted to substitutionally dope TiO_2 by nitrogen and succeeded in his pursue due to the mixing of the p states of nitrogen with O p states [110]. Using VASP with cut-off energy of 29 Ry and Vanderbilt psedopotentials, Kamisaka et al. performed theoretical studies on carbon doped TiO_2 through investigating the electronic bandstructure and optical properties [111]. Meng

et al. utilized VASP with the DFT+U framework to unravel the effect of Ti and Cu doping in the enhancement of the bandgap of α-Fe_2O_3 as shown in **Figure III-1** [112].

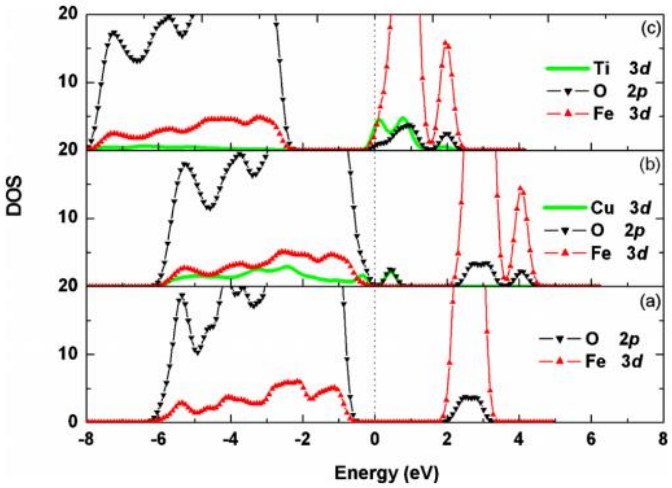

Figure III-1 (a) The DOS for bare α-Fe2O3 (b) The DOS of Cu-doped α-Fe2O3 (c) The DOS of Ti-doped α-Fe2O3.

3.2.2 Charge carrier transport

Charge carrier transport and electron-hole separation can be evaluated via DFT. Deskins et al. employed CP2K package with norm-conserving pseudopotentials to study the effect of adding excess electron to pristine TiO_2 and hydroxylated TiO_2 at (110) surfaces [113]. Kleiman-Shwarsctein et al. exploited VASP with LDA-DFT and cut-off energy of 400 eV to elucidate the effect Al doping in α-Fe_2O_3 to improve the conductivity [114].

3.2.3 Electrochemical surface reactions and reaction mechanism

DFT plays an important role in predicting the characteristics of the interface between the liquid and SC is of great significance for the understanding of the PEC water splitting performance for a given SC-liquid combination [3]. Valdes, Rossmeisl and Norskov groups devised an electrochemical framework to probe the photo-oxidation of water via DFT [115–117]. Within this framework, the thermodynamics of the interface reactions can offer a wholistic atomistic explanation for the PEC water splitting. DFT can also give a hand in the determination of the reaction pathways and mechanism for PEC water splitting. As a function of electrode potential, Skulasson et al. calculated the activation energy of hydrogen evolution reaction

(HER) with nudged elastic band (NEB) calculations wit RPBE exchange-correlation functional [118].

3.3 Metal oxides for PEC water splitting applications

Numerous of material classes were investigated for PEC water splitting applications such as carbon-based SCs, oxynitrides, classic SCs, chalcogenides. However, the most popular material class for photoanodes is metal oxides [24]. Among this class, α-Fe_2O_3 (haematite), WO_3 (tungsten trioxide) and $BiVO_4$ (bismuth vanadate) are heavily studied materials but TiO_2 (titantia) is the most investigated material being the first material to be utilized in PEC water splitting [23]. Metal oxides are known to be very stable in aqueous and illuminated conditions. Yet, they suffer from large bandgaps and poor conductivity. Doping is one of the most established techniques to mitigate theses deficits in metal oxides. A myriad of dopants and defects in metal oxides were explored for water splitting applications.

Hufnagel et al. used VASP with PAW pseudopotentials and DFT+U approach to explore the effect of tin-doping in α-Fe_2O_3 photoanode for PEC water splitting applications. The study revealed through the calculations of energetics of surface intermediates for OER that tin-doped α-Fe_2O_3 decreased the overpotential on (0001) facet. Also, the study showed that tin-doped α-Fe_2O_3 enhanced the charge transfer efficiency [119].

Chandrasekaran et al. combined experimental and computational approach to unveil the effect of Mn and V doping in WO_3 for PEC water splitting applications. In this study, VASP was used with Vanderbilt (ultrasoft) pseudopotentials. The study showed that Mn and V doping reduced the overpotential. Furthermore, the doped WO_3 improved photocurrent densities by 1.8 and 4.1 times for Mn and V, respectively [120].

Concerning $BiVO_4$, Wen et al. employed CASTEP within the PBE-GGA framework with ultrasoft pseudopotentials to investigate the effect of F doping in monoclinic $BiVO_4$. The

study revealed that the bandgap was narrowed and the separation of the photoexcited electron-hole pair was enhanced [121]. While, Zhao et al. exploited CASTEP with PBE-GGA and LDA+U combined with experiments to clarify the roles of O vacancies in W-doped $BiVO_4$. The study showed enhanced separation of photogenerated electron-hole pair [122].

Regarding TiO_2, Lin et al. used DFT+U on VASP software to evaluate the co-doping effect of Fe and Ni in TiO_2 as shown in **Figure III-2** [123]. It was found that co-doping improved the optical absorption of TiO_2 within the visible region [123].

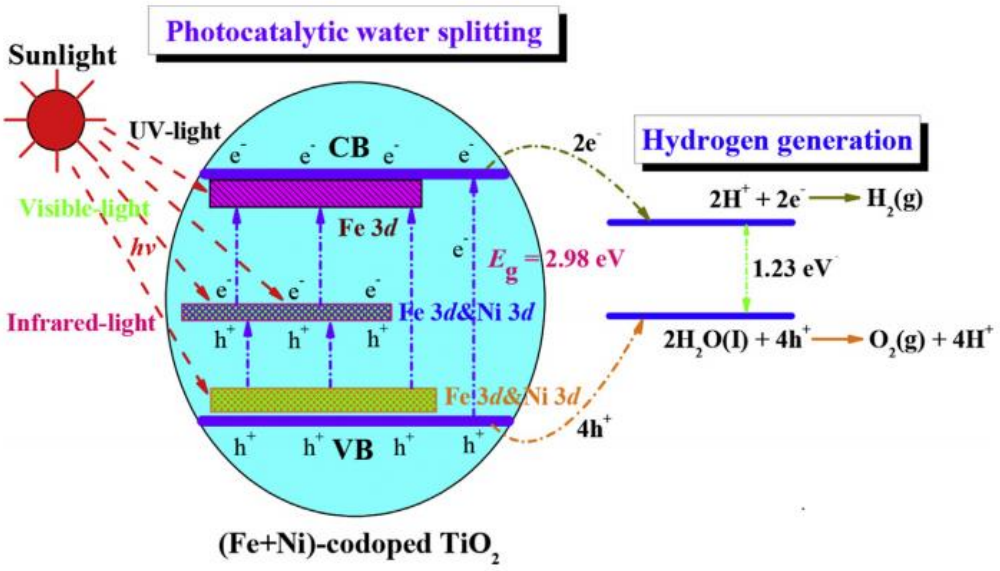

Figure III-2 PEC water splitting mechanism for TiO_2 co-doped with Fe and Ni.

Opoku et al. employed CASTEP within the DFT+U framework to the study the optical properties, electronic and the synergistic effects of ternary doping (Fe/C/S) of anatase TiO_2 [124].

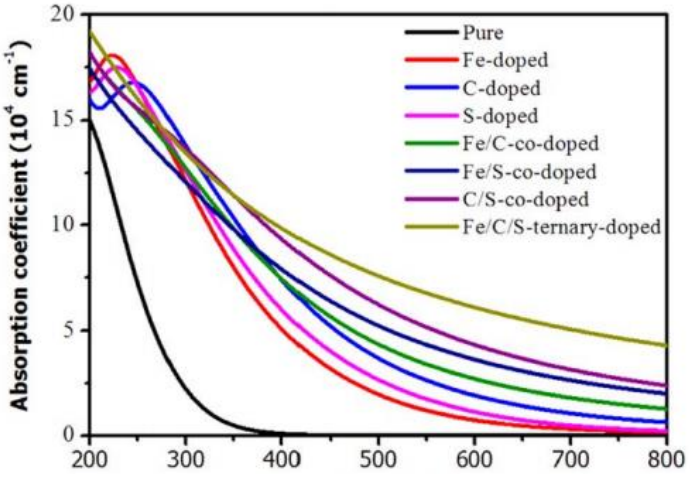

Figure III-3 The absorption coefficient of different dopants in anatase TiO_2.

The study showed that the ternary doped TiO_2 is more favourable under oxygen-rich conditions, the absorption of ternary doped TiO_2 was enhanced over the visible region as shown in **Figure III-3** [124]. Also, band edge positions relative the redox potential of water species are excellent.

Shi et al. utilized the DFT+U approach on VASP to study the effect of C-Nd monodoping and co-doping in anatase TiO_2. The study exhibited the reduction of recombination of the photogenerated electron-hole pairs that improved the photocatalytic activity for solar-driven hydrogen production [125].

Among the various dopants, carbon doping in titania raised a huge controversy in literature whether it can induce visible light absorption or not. Khan et al. claimed that carbon doping in titania resulted in unprecedented efficiency of 8.35 % [126] whereas Lackner, Fujishima and Murphy criticized the study and attributed the flawed result to the erroneous measurement protocol of evading the placement of AM 1.5 filter and the underestimation of the bias voltage [17–19]. Nevertheless, numerous experimental and computational studies showed promising results of specific carbon defects in titania for water splitting applications [38–44].

3.4 Zirconia for PEC water splitting applications

Similar to titania, zirconia is a wide-gap metal oxide with distinctive properties such as high melting-point, chemical inertness and high corrosion tolerance [45] that render it advantageous for a plethora of applications such as biomedical implants, solid oxide fuel cells, dental applications, and other applications [28-49]. However, the bandgap of zirconia needs to be optimized to enhance its photocatalytic activity. Unlike titania, the use of zirconia in water splitting systems has been poorly addressed in literature. A few studies shed the light on the effect of various dopants on the performance of zirconia in solar-driven hydrogen production systems. Hernandez et al. attempted experimentally to dope ZrO_2 with Ce and Er [68]. The study revealed superior photocatalytic activity compared to pure zirconia. The authors attributed this

improvement in the performance due to the increased charge carrier separation and the ability of Ce and Er doped zirconia to absorb visible light. While, Tolba et al. addressed various H doping scenarios in zirconia using DFT+U and ultrasoft pseudopotentials on CASTEP. This work revealed that at high oxygen vacancies, H_O-O_V improved the dielectric constant and improved the optical absorption as shown in **Figure III-4** [69]**.**

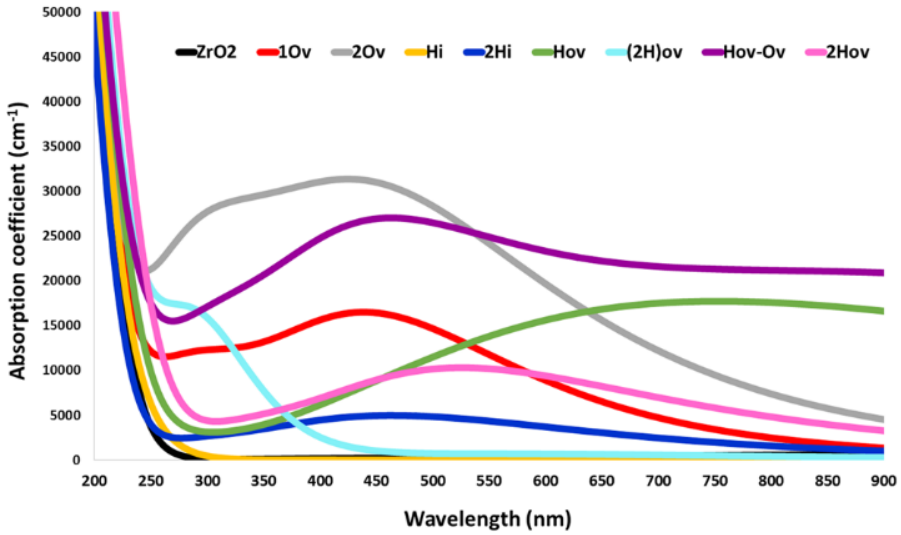

Figure III-4 The optical absorption for m-ZrO_2 compared with the different H doping scenarios.

On the other hand, Gul et al. applied PBEsol-GGA DFT as implemented in CASTEP to scrutinize the effect of concentration of Ce doping in zirconia. The study revealed that 6 % Ce doping gave the highest bandgap minimization as shown in **Figure III-5** [130].

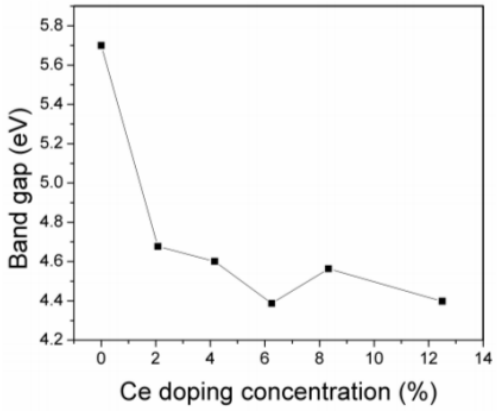

Figure III-5 The effect of varying the the Ce doping percentage in zirconia in the minimization of the bandgap.

Carbon-doped zirconia was briefly investigated in the literature [80–82]. Ding et al. utilized CASTEP with Ceperley-Alder-perdew-Zunger (CA-PZ) LDA as exchange correlation functional to investigate the effect of C and N doping in cubic zirconia (c-zirconia) [80]. The study focused only on anion doping with 4.17% doping concentration. The study showed that doped zirconia gave 2.3 eV and 2.8 eV in case of C and N, respectively. Moreover, C doping enhanced the visible light absorption, and the static dielectric function. In another study, Zhang et al. shed the light on the doping and co-doping of c-ZrO_2 with C and F [81]. The study concluded that C-doped c-ZrO_2 gave the highest bandgap minimization. The authors employed DFT+U as implemented on CASTEP with Vanderbilt ultrasoft pseudopotentials. Finally, Tailor et al. investigated the effect of N and C doping in tetragonal and monoclinic ZrO_2 from a general thermodynamic point of view [82]. The study showed that C doping has low formation energies which indicates the easiness of C incorporation within the ZrO_2 crystal. This work used HSE hybrid functionals on VASP software. However, in conclusion, the debateable effect of carbon doping in zirconia was neither treated nor unriddled systematically and comprehensively for water splitting applications.

3.5 DFT for quantum capacitance calculations of carbon electrodes

Since C_Q has been the of great interest to the development and enhancement of carbon electrodes. Research have looked forward for designing and investigating different graphene allotropes using C_Q. Wood et. al. have used the PBE method with ultrasoft pseudopotential to investigate the C_Q of the pristine graphene along with doped graphene and strained graphene [131]. For the study of doped graphene, point defect and substitution was performed in a unit cell of 54 atoms. While for the stress effect, rippled graphene sheet of 32 atoms was used. The rippling of the graphene sheet was applied such as the in-plane lattice parameter was decreased convoluting the out of plane lattice parameter with a sinusoidal variation. Their results revealed that when comparing the C_Q of the defected graphene (Stone-Wales, divacancies and

monovacancies), the divacancy gave a large DOS around the E_F and hence a high C_Q. On the other hand, the Stone-Wales and the monovacancy enhanced the C_Q by a very low factor. Furthermore, by adding H, N, and O to the monovacancy, the DOS along with the C_Q changed dramatically around the PZC and gave a much higher C_Q values. Moreover, the doping of graphene with N and B increased the C_Q values. However, the effect of dopants also affected the position of enhancement of the C_Q values according to the potential window. It was found that the N-doping enhanced the C_Q of graphene in the negative potential window, while the boron doping enhanced the C_Q of graphene in the positive potential window. This was attributed to the increase of the DOS of the related electronic structures relative to the E_F. Upon folding the graphene sheet, the PDOS of the carbon atoms along the folded edge changes as presented in **Figure III-6 (b).** This impacted the resulted C_Q and caused an enhancement in the total capacitance performance of the graphene as presented in **Figure III-6 (a)** [131].

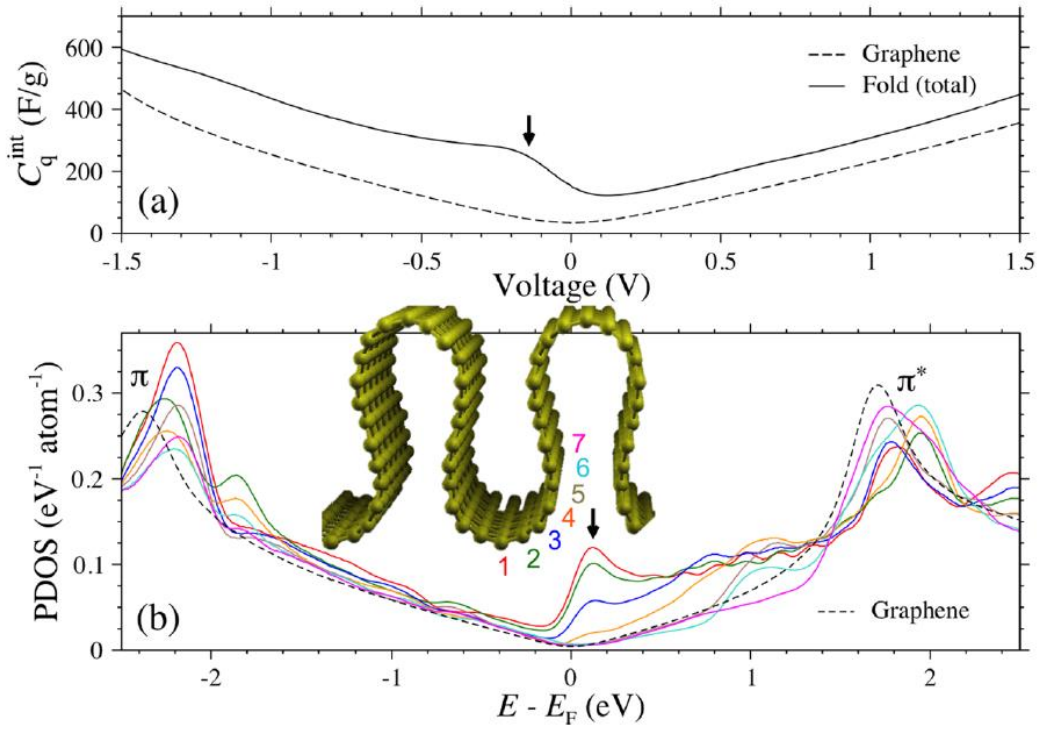

Figure III-6 (a) C_Q of folded graphene Vs. pristine graphene, and (b) PDOS of the seven carbon atoms along the folded edge of the folded graphene.

The point defects in graphene were also in-depth investigated by Pak et.al., they found that the C_Q was enhanced dramatically due to the delocalization of electrons near the EF that increased the DOS and hence the C_Q value around the PZC [132]. Further investigation of graphene defects was investigated over the course of research in order to illustrate the best defected structure that can be adopted in experimental work. To this end, Yang et. al. have used the PBE method to study N-defected graphene. The study included quaternary doped graphene, three N-dopants with one vacancy, pyridinic-N doping, and single vacancy. The study also included different concentrations of the single vacancy and the N-doping. It was found that the vacancies and the N-doping caused the accumulation of charge carriers near the E_F and hence increased the relative DOS. This caused an increase in the corresponding C_Q. It was also observed that with increasing the concentration of either the vacancies or the N-dopants, the C_Q around the PZC increased [133]. Other dopants such as Si, S, and P were compared to the N-dopant in their effect on C_Q of graphene [134]. As presented on **Figure III-7 (a)**, the P-doping increased the C_Q around the PZC dramatically in comparison to other dopants while Si and S did not have a great impact on the C_Q of the graphene. On the other hand, when combining different N-doping positions with the other dopants the effect changed. It can be observed from **Figure III-7 (b)** that the S doping with graphitic N-doping increased the C_Q greatly in the negative potential window, while the Si doping with graphitic N-doping increased the C_Q around the PZC. However, the combination between the pyrrolic N-doping and the Pyridinic N-doping with the P, Si, and S doping did not have a great impact on the enhancement of the C_Q in comparison to the pare N-doping [134]. C_Q has also been used in calculating the capacitance performance of hybrid electrodes. Mohsin et. Al. have studied the C_Q of hybrid graphene/Cu sheets [135]. The study included the modelling of three layers of Cu <111> plane with a monolayer of graphene. It was observed that the C_Q of pristine graphene increased greatly which was attributed to the weakening of the e-e interaction and Fermi velocity modulation [135]. Recent researchers are using graphene oxide instead of graphene in supercapacitor application since it keeps the 2D shape of graphene and provide a higher conductivity due to the presence of oxygen atoms. Song

et. Al. have studied the effect of the oxygen functional groups that forms in case of graphene oxide on the C_Q values of the pristine graphene. The study focused on the epoxy and hydroxyl groups. It was found that both functional groups enhanced the C_Q values against the pristine graphene. However, the hydroxyl group had a much greater effect than the epoxy functional group [136]. In summary, the DFT can give a great insight on the proper electrode material to be used in supercapacitor electrodes. However, more screening of materials is required to provide a library of the C_Q values of the desired carbon materials that will allow a fast-cheap method to choose the right electrode material for the perfect supercapacitor performance.

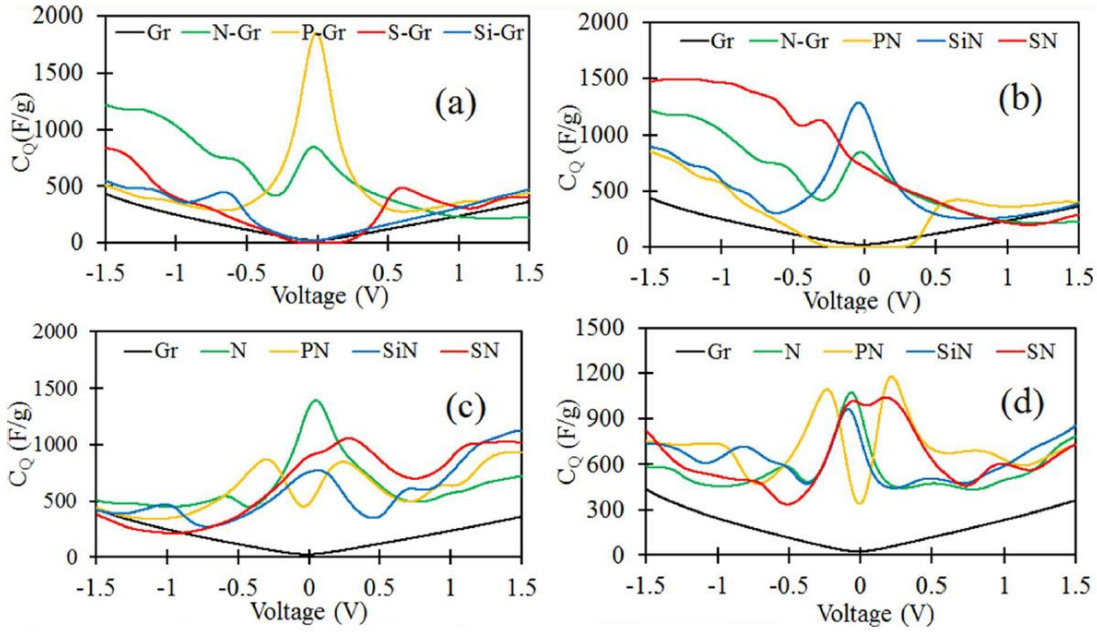

Figure III-7 Change of C_Q of graphene upon doping by: (a) different doping elements in graphene sheet, (b) Graphitic N along with other dopants, (c) pyridinic N along with other dopants, (d) pyrrolic N along with other dopants.

Chapter IV : Methods

4.1 Computational details for carbon-defected zirconia for water splitting

In our study, CASTEP code [137] was utilized for the spin-polarized density functional theory (DFT) calculations. For modelling the electron-electron interaction, the PBE-GGA (Perdew-Burke-Ernzerhof of Generalized Gradient Approximation) [16] was chosen. The Ultrasoft-pseudopotential [138] was adopted to account for the electron-ion interaction. In the framework of plane-wave basis set, the Kohn-Sham wave functions of electrons were expanded up to 380 eV. In consideration of the irreducible Brillouin zone, the Monkhorst-Pack scheme [139] was implemented to sample the k-points where a mesh of (5x5x5) and (2x5x5) (0.04 spacing of points) k-points were constructed for the single unit cell and the supercell, respectively. Both were used for geometry optimization calculations and generation of density of states (DOS) profile. In order to remedy the self-interaction error in DFT [140], the Hubbard correction approach [141] was employed to describe the energy bandgap adequately. Furthermore, Hubbard correction was exploited to attain proper positions of the defect states within the bandgap and to improve the accuracy of the defect formation energy calculations [142]. In this regard, the applied Hubbard U parameters, were 4 eV to the 4d orbitals of Zr and 4 eV on the 2p orbitals of O to maintain the nature of Zr-O covalent bond as explained in ref. 143. Concerning the geometry optimization convergence criteria, the mean Hellmann-Feynman force was set to 0.01 eV/A while the maximum displacement tolerances, maximum stress, and energy change were adjusted to 5.0×10^{-4}, 0.02 GPa, and 5.0×10^{-6} eV/atom, respectively. In pursuance of benchmarking of the structures and computational setup, the coordinates of the atoms and the lattice parameters of m-ZrO_2 were acquired from Purohit et al. work [144] and the calculated parameters were compared to their counterparts in literature. After structural relaxations, the obtained energy bandgap and lattice parameters matched the previously reported experimental and

theoretical values [145]. The values were E_g=5.14 eV, a =5.24 Å, b=5.20 Å, and c=5.40 Å, respectively. Hence, the computational setup was accredited to be inherited in the optimization of the defected structures. For the sake of studying all the possible carbon defected structures, a (2x1x1) supercell including 24 atoms was established to embrace the different defect concentrations and to minimize the electrostatic interaction with the periodic images. Additionally, two defect concentrations were taken into consideration to represent the low and high concentrations specifically; 0.125 and/or 0.25 nD/nZr (D=defect) where one and/or two defects were introduced to the supercell. It is noteworthy that m-ZrO_2 has two inequivalent oxygen sites of different binding energies namely; three-coordinated (O_{3c}) and four-coordinated (O_{4c}). Initially, the oxygen-deficient (reduced) ZrO_2 was simulated in two scenarios with 0.125 and 0.25 V_O defects following the approach of Sinhamahapatra et al. [146]. Afterwards, interstitial, substitutional, and complex carbon defects were incorporated into the pristine and the reduced ZrO_2 as described by the defects equations in **Table V-1**. Starting from the optimized pristine structure, the following structures were modelled: (i) C_{O3c} (carbon atom substituted O_{3c}), (ii) C_{O4c} (carbon atom substituted O_{4c}), (iii) C_{O3c} - C_{O3c} (two adjacent bonded C_{O3c}), (iv) C_{O3c}=O_{3c} (C_{O3c} bonded with adjacent O_{3c}) and (v) C_i (carbon atom placed between two adjacent O_{3c} and O_{4c}). With respect to the structures which started from the optimized reduced ZrO_2, the subsequent configurations were studied: (vi) C_{Vo3c} (carbon atom occupied O_{3c} vacancy), (vii) C_{Vo4c} (carbon atom occupied O_{4c} vacancy), (viii) $V_{O4}C_{O3c}$ (V_{O4c} associated with C_{O3c}), and (ix) $V_{O4c}C_i$ (V_{O4c} associated with C_i). Other calculations started from m-ZrO_2 defected with C_{O3c} such as: (x) $C_{O3c}V_{O3c}$ (C_{O3c} associated with V_{O3c}) (xi) $C_{O3c}V_{O4c}$ (C_{O3c} associated with V_{O4c}) while the last structure started from m-ZrO_2 with interstitial carbon defect; (xii) C_iV_{O4c} (C_i associated with V_{O4c}). It is obvious that (i) is identical to (vi), (ix) is identical to (xii) and (viii) is identical to (xi), albeit the starting structures are different. The defect formation energy was calculated to assess the relative difficulty of introducing the defects into the

structure. Apart from this, binding energy was also computed for complex (associated) defects as an essential thermodynamic stability indicator against their decomposition into their rudimentary defects [147]. The formation energy of a given neutral defect (D) is denoted by E_D^f and can be defined as:

$$\boldsymbol{E_D^f} = E_{defected} - E_{pristine} + \sum_i \Delta \boldsymbol{n_i} \mu_i \qquad \text{(IV-1)}$$

where $E_{defected}$ and $E_{pristine}$ represent the calculated total energies of the defected supercell and the pristine supercell, respectively, Δn_i is the difference between the number of a given species i in the pristine supercell and the number of the same species in the defected supercell. Eventually, μ_i symbolizes the chemical potential of a given species i. The chemical potential calculations depend on the thermodynamic reservoir of the added/removed species and the experimental growth conditions that may be oxygen-rich or zirconium-rich as extreme conditions. For oxygen-rich (zirconium-poor) condition, μ_O can be obtained from ground state energy of oxygen molecule whereas μ_{Zr} and μ_C can be calculated from $\mu_{Zr} = \mu_{ZrO2} - 2\mu_O$ and $\mu_C = \mu_{CO2} - 2\mu_O$, respectively. Under the zirconium-rich (oxygen-poor) condition, μ_{Zr} can be acquired from ground state energy of single zirconium atom in bulk zirconium while μ_O can be provided by $\mu_O = (\mu_{ZrO2} - \mu_{Zr})/2$ then μ_C can be estimated via $\mu_C = \mu_{CO2} - 2\mu_O$. On the other hand, the binding energy of a given complex C is expressed by E_b and its formula is:

$$E_b = E_C^f - \sum_l E_D^f \qquad \text{(IV-2)}$$

where E_C^f and E_D^f are the formation energies of a given complex and the formation energy of a defect that constitutes the complex C, respectively. The number of l species equals the number of defects composing the given complex.

The complex dielectric function (ε) can be described as [148]:

$$\varepsilon = \varepsilon_1 + i\varepsilon_2 = N_2 \qquad \text{(IV-3)}$$

where ε_1 and ε_2 are the real and imaginary parts of the dielectric constant, respectively. The calculation of the imaginary part of the dielectric function is estimated using the following relationship [148]:

$$\boldsymbol{\varepsilon_2(\omega)} = \frac{2e^2\pi}{\Omega\varepsilon_0}\sum_{k,v,c}|\langle\boldsymbol{\varphi_k^c}|\boldsymbol{H'}|\boldsymbol{\varphi_k^c}\rangle|^2\boldsymbol{\delta}(\boldsymbol{E_k^c}(\overrightarrow{\boldsymbol{k}}) - \boldsymbol{E_k^v}(\overrightarrow{\boldsymbol{k}}) - \hbar\boldsymbol{\omega}) \qquad \text{(IV-4)}$$

where Ω is the unit cell volume, $\hbar\omega$ is the photon energy, H' is the matrix element for the electromagnetic perturbation added to the normal Hamiltonian taken between the valence and conduction band Bloch states at wave vector $(\overrightarrow{k})$, and the δ -function is the energy conservation at $(\overrightarrow{k})$. In particular, the imaginary part is calculated first, from which the real part $\varepsilon_1(\omega)$ can be obtained by the Kramers–Kronig transform, using the fact that the dielectric constant describes a causal response. The dielectric constant $\varepsilon(\omega)$ is a function of the frequency (ω), classifying ε into the electronic contribution part $(\varepsilon_{\omega\to\infty})$, and the lattice vibrational contribution part $(\varepsilon_{\omega=0})$, or the optical and static molecular polarizability. Based on the calculated dielectric constants (refractive index n(ω), extinction coefficient k(ω), absorption coefficient α(ω), reflectivity R(ω), and the energy-loss spectrum L(ω)), the other optical properties can then be obtained using the following relationships [148]:

$$\boldsymbol{n(\omega)} = \frac{\left[\sqrt{\varepsilon_1^2(\omega)+\varepsilon_2^2(\omega)}+\varepsilon_1(\omega)\right]^{0.5}}{\sqrt{2}} \qquad \text{(IV-5)}$$

$$\boldsymbol{k(\omega)} = \frac{\left[\sqrt{\varepsilon_1^2(\omega)+\varepsilon_2^2(\omega)}-\varepsilon_1(\omega)\right]^{0.5}}{\sqrt{2}} \qquad \text{(IV-6)}$$

$$\boldsymbol{\alpha(\omega)} = \sqrt{2}\boldsymbol{\omega}\left[\sqrt{\boldsymbol{\varepsilon_1^2(\omega)+\varepsilon_2^2(\omega)}}-\boldsymbol{\varepsilon_1(\omega)}\right]^{0.5} \qquad \text{(IV-7)}$$

$$\boldsymbol{R(\omega)} = \left|\frac{\sqrt{\varepsilon_1(\omega)+j\varepsilon_2(\omega)}-1}{\sqrt{\varepsilon_1(\omega)+j\varepsilon_2(\omega)}+1}\right|^2 \qquad \text{(IV-8)}$$

$$\boldsymbol{L(\omega)} = \frac{\varepsilon_2(\omega)}{[\varepsilon_1^2(\omega)+\varepsilon_2^2(\omega)]} \qquad \text{(IV-9)}$$

4.2 Computational details for quantum capacitance for carbon-based electrodes

Carbon materials generate capacitance depending on the adsorption/desorption at the electrode/electrolyte interface. The capacitance generated from the electrolyte is directed by the accumulation of the charge and is affected by the ion concentration. On the other hand, the capacitance generated from the electrode is limited by the quantum effect resulted from the electrode material [149]. For carbon electrodes, the EDL capacitance is affected by the pore size, pore shape, and the total surface area. While the electronic behaviour of the electrode is controlled by the C_Q. The electronic reaction of the electrode material results in an electronic contribution to the capacitance performance of the Helmholtz layer at the electrode/electrolyte interface. To this end, the total capacitance (C_T) of a carbon electrode can be evaluated from both the EDL capacitance and quantum capacitance and can be calculated using **eq. IV-10** with ignoring any redox or pseudo-capacitance effect [131].

$$\frac{1}{C_T} = \frac{1}{C_Q} + \frac{1}{C_{DL}} \qquad \text{(IV-10)}$$

where C_{DL} is the double layer capacitance, which combines both the diffuse layer and the Helmholtz layer. The C_Q can be estimated for EDL electrodes according to two proposed scenarios using the electronic structure of the electrode material [131,136]. Metals that can acquire high DOS, does not possess a great change due to removing or adding electrons, hence their chemical potential (μ_e) does not vary very much and the C_T is a function of C_{DL} only. On the other hand, for semiconductors with low DOS, any change in the charge carriers can affect the electrode potential dramatically [150]. Therefore, the C_Q plays a major role in detecting the capacitance of 2D semiconductors. The C_Q is defined as the ratio between the variation of charge (dQ) and electrode potential (dV) namely differential electrode potential [131,133,136]. **Eq. IV-11** represents the relation to calculate the C_Q^{diff} from DOS assuming uncharged electrode [131,136,151,152].

$$C_Q^{diff} = \frac{dQ}{dV} = e^2 DOS(-Ve) \qquad \text{(IV-11)}$$

where DOS is the electronic density of states, *e* is the elementary charge, and (-Ve) refers to the relative electronic density with respect to E_F. The previous equation can be used in bulk materials. While for 2D materials, the C_Q^{diff} can be represented by **eqs. IV-12** and **IV-13** [132–134,153,154].

$$C_Q^{diff} = \frac{dQ}{dV} = e^2 \int_{-\infty}^{+\infty} DOS\ F_T(E-\mu)dE \quad \text{(IV-12)}$$

$$F_T(E) = (4k_BT)^{-1} Sech^2(\frac{E}{2k_BT}) \quad \text{(IV-13)}$$

where μ is the electrochemical potential, E is the relative energy with respect to E_F, and $F_T(E)$ is the thermal broadening function. Another equation was established to calculate the C_Q^{diff} for pristine graphene without taking temperature into consideration (**eq. IV-14**) [131,133].

$$\boldsymbol{C_Q^{diff} = \frac{dQ}{dV} = e^2 \frac{g_s g_v}{2\pi(\hbar V_F)^2} |\mu|} \quad \text{(IV-14)}$$

where V_F is the Fermi velocity of carriers (~108 cm/s), g_s is the spin degeneration (=2), and g_v is the valley degeneration (=2).

For modelling carbon structures and demonstrating quantum capacitance, VASP [155] (Vienna Ab-initio Simulation Package) software was utilized for the DFT calculations [156]. For the exchange-correlation scheme, the PBE-GGA (Perdew Burke-Ernzerhof of Generalized Gradient Approximation) [157] was chosen to model the electron-electron interaction. The PAW pseudopotentials[158,159] (Projector augmented-wave) were adopted to account for the electron-ion interaction. In the framework of plane-wave basis set, the Kohn-sham wave functions were expanded with a kinetic energy cut-off of 800 eV for both geometry optimizations and total energy calculations. The Monkhorst-pack method was used to treat the sampling of k-points in the Brillouin zone and the generation of Density of States (DOS) profile. The Monkhorst-pack grids were set to 31x31x9, 31x31x1, and 1x1x16 for graphite, graphene, and CNT, respectively. For generation of DOS, Methfessel-Paxton smearing scheme was applied with a broadening factor of 0.2 eV. For graphite, the VdW-DF2 non-local correlation functional[160] was implemented to account for the dispersion interactions result from Van der Waals forces between the graphitic layers. For CNT, the

chirality of the was (11,0). A 25x25 Å vacuum slab was introduced for the CNT in the X and Y directions while a 20 Å vacuum slab was constructed in the Z-direction to avoid the periodic image interactions. The resulted curves of the quantum capacitance were smoothed using the Adjacent-Averaging method.

For the NDG study, A (5x5x1) graphene supercell was established to encompass the three different combined types of N-defects. A kinetic energy cut-off of 600 eV for both geometry optimizations and total energy calculations. The Monkhorst-pack method was adopted to sample the k-points in the Brillouin zone and the generation of Density of States (DOS) profile. The Monkhorst-pack grids were set to 31x31x1, and 15x15x1 for graphene, and NDG, respectively. For generation of DOS, gaussian smearing was applied with a broadening factor of 0.05 eV. A 20 Å vacuum slab was constructed in the Z-direction for both materials to avoid the periodic image interactions.

Chapter V : Carbon Defects in Zirconia for Water Splitting

The impact of the various carbon defects in pristine and reduced m-ZrO_2 was investigated in light of the modification in electronic and optical properties.

5.1 Defect energetics

Before delving into the electronic and optical properties, analysing the relative thermodynamic stability of the defects in the doped structures is crucial through the comparison of the formation energies of the defects and the binding energies of the complex defects. The formation energies of the studied structures are listed in **Table V-1** at 100 K and 1000 K. Generally, from a thermodynamic point of view, formation energies of carbon defects are more favourable under oxygen poor condition at both high and low temperatures. Thus, the discussion would focus only on poor oxygen condition. For carbon-substituting-oxygen structures, it was found that carbon substituting O_{3c} atom is energetically more stable than substituting O_{4c} atom. Concerning carbon interstitial defect, it was observed to have the highest formation energy. Regarding complex defects formed in pristine, it was noticed that forming a complex of two adjacent C_{O3c} defects with a single bond between the two carbon atoms is more favourable to exist rather than lone C_{O3c} defect where C_{O3c} - C_{O3c} (iii case) has the lowest formation energy at 1000 K. In addition, the formation of double bond between C_{O3c} defect and its adjacent O_{3c} atom was identified as more stable complex than lone C_{O3c} defect with a difference in their formation energies reaching -0.12 eV.

Upon addressing the effects of carbon defects on inducing oxygen vacancies, it was reported in the group previous study that formation of V_{O4c} is prevalent over formation of V_{O3c} [69]. However, in this study, it was found that the presence of C_{O3c} atom initiates the formation of adjacent V_{O3c} that is more likely to occur than the formation of V_{O4c} with a difference in their

formation energies equals to -1.75 eV. This may be attributed to the fact that V_{O3c} bonding environment is more preferred for carbon since carbon can form either a double bond with O_{3c} (iv case) or a complex with adjacent C_{O3c} (iii case). Also, the formation energy of V_{O4c} with a prior existence of C_i equals -2.5 eV which renders interstitial carbon defects effectively induce the formation of oxygen vacancies within m-ZrO_2, exothermally, in contrast to the formation of oxygen vacancies in m-ZrO_2 that have positive formation energies. It is also reported that the formation of C_i is easier in case of oxygen-deficient m-ZrO_2 than in pristine m-ZrO_2 crystal. Moreover, calculations indicated that C_{VO3c} is more thermodynamically possible than C_{O3c}. Finally, the formation of C_{O3c} adjacent to V_{O4c} (viii case) was found to be more likely to occur than the formation of C_{O3c} in pristine m-ZrO_2. Generally, the considered fabrication conditions (oxygen-rich or -poor) and the temperature have a significant impact on the formation energy of the defected structures. In summary, a conclusion can be reached from **Table V-1** that elevating the temperature promotes and facilitates the formation of carbon defects and complex defects, and especially in O-poor condition where the percentage of decrease in formation energies from 100 to 1000 K is significant.

Table V-1 Formation energy (E_D^f) of all defected m-ZrO_2 structures.

Initial structure	Defect	Formation Energy (E_D^f) (eV)				Equations of defects
		O-rich		O-poor		
		100 K	1000 K	100 K	1000 K	
m-ZrO_2	(i) C_{O3c}	14.46	12.95	2.45	0.94	$CO_2(g) + O_{O3c}^x \rightarrow C_{O3c}'''' + \frac{3}{2}O_2(g) + 2h^\bullet$
	(ii) C_{O4c}	14.67	13.16	2.66	1.15	$CO_2(g) + O_{O4c}^x \rightarrow C_{O4c}'''' + \frac{3}{2}O_2(g) + 2h^\bullet$
	(iii) C_{O3c} - C_{O3c}	23.82	20.80	-0.20	-3.22	$2CO_2(g) + 2O_{O3c}^x \rightarrow 2C_{O3c}'''' + 3O_2(g) + 4h^\bullet$
	(iv) C_{O3c} =O_{3c}	14.34	12.83	2.33	0.82	$CO_2(g) + O_{O3c}^x \rightarrow C_{O3c}'''' + \frac{3}{2}O_2(g) + 2h^\bullet$
	(v) C_i	12.00	11.50	3.99	3.50	$CO_2(g) + V_i^x \rightarrow C_i'''' + O_2(g) + 4h^\bullet$
Oxygen-deficient m-ZrO_2	(vi) C_{VO3c}	8.55	8.07	0.55	0.07	$CO_2(g) + V_{O3c}'' \rightarrow C_{O3c}'''' + \frac{1}{2}O_2(g) + 2h^\bullet$
	(vii) C_{VO4c}	8.66	8.17	0.65	0.17	$CO_2(g) + V_{O4c}'' \rightarrow C_{O4c}'''' + \frac{1}{2}O_2(g) + 2h^\bullet$
	(viii) $V_{O4c}C_{O3c}$	13.16	11.65	1.16	-0.35	$V_{O4c}'' + CO_2(g) + O_{O3c}^x \rightarrow V_{O4c}C_{O4c}'''' + \frac{3}{2}O_2(g) + 2h^\bullet$
	(ix) V_{O4c} C_i	8.50	8.03	0.51	0.03	$V_{O4c}'' + CO_2(g) + V_i^x \rightarrow V_{O4c}C_i'''' + O_2(g) + 2h^\bullet$

C_{O3c} defected m-ZrO_2	(x) $C_{O3c}V_{O3c}$	2.97	1.94	-1.04	-2.06	$CO_2(g) + O_{O3c}^x + V_{O3c}'' \rightarrow C_{O3c}V_{O3c}'''' + \frac{3}{2}O_2(g) + 2h^\bullet$
	(xi) $C_{O3c}V_{O4c}$	4.70	3.69	0.71	-0.31	$CO_2(g) + O_{O3c}^x + V_{O4c}'' \rightarrow C_{O3c}V_{O4c}'''' + \frac{3}{2}O_2(g) + 2h^\bullet$
C_i defected m-ZrO_2	(xii) C_iV_{O4c}	2.53	1.51	-1.47	-2.50	$CO_2(g) + V_i^x + V_{O4c}'' \rightarrow C_iV_{O4c}'''' + \frac{3}{2}O_2(g) + 2h^\bullet$

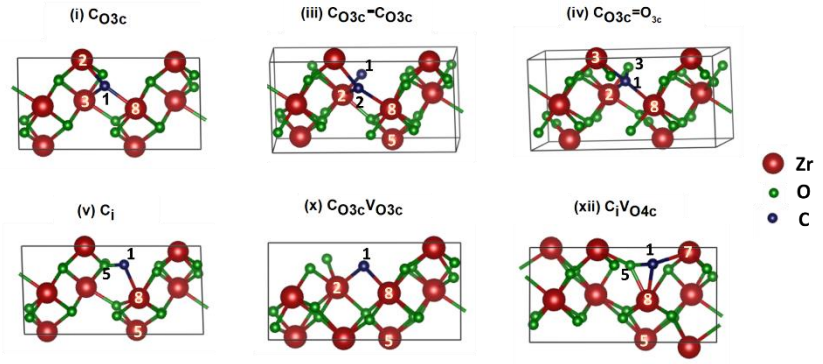

Figure V-1 Crystals structures for the short-listed defected structures.

The binding energies presented in **Table V-2** reflects the thermodynamic stability of studied complexes against dissociation over the wide range of temperature variation and regardless the considered experimental growth conditions (O-rich/-poor). Additionally, binding energies of complex defects depend on the pathway of their formation. For example, V_{O4c} C_i and V_{O4c} C_{O3c} have more positive binding energies than C_i V_{O4c} and V_{O4c} C_{3c}, respectively, although the final defected structures are the same.

Table V-2 Binding energies (E_b) for complex defects.

Initial structure	Defect	Binding Energy (E_b) (eV)			
		O-rich		O-poor	
		100 K	1000 K	100 K	1000 K
m-ZrO_2	(iii) C_{O3c} - C_{O3c}	-5.10	-5.10	-5.10	-5.08
Oxygen-deficient m-ZrO_2	(ix) V_{O4c} C_i	-9.40	-8.35	-6.45	-5.42
	(viii) V_{O4c} C_{O3c}	-7.20	-6.18	-4.26	-3.24
C_{O3c} defected m-ZrO_2	(x) $C_{O3c}V_{O3c}$	-17.29	-15.79	-5.29	-3.77

C_i defected	(xi) $C_{O3c}V_{O4c}$	-15.66	-14.14	-4.71	-3.20
m-ZrO_2	(xii) C_iV_{O4c}	-15.37	-14.87	-8.43	-7.95

In the present-day study, the scope of further discussion would be focused on the subsequent defected structures: (i), (iii), (iv), (x), (xii), and (v), for the following reasons. First, the defected structures (i), (ix), and (viii) are identical to (vi), (xii), and (xi), respectively. Second, the E_D^f of (i) C_{O3c} < (ii) C_{O4c}, and the E_D^f of (x) $C_{O3c}V_{O3c}$ < (xi) $C_{O3c}V_{O4c}$. Third, (iii), and (iv) were the most thermodynamically favourable defects in pristine m-ZrO_2. Lastly, (v) would be also examined for the sake of comprehensive scanning of carbon defects in m-ZrO_2. The structural parameters of the selected defected structures are listed in **Table V-3** and depicted in **Figure V-1**. It was observed that the defected structures introduced distortions to the m-ZrO_2 crystal in terms of increasing the lattice volume and modifying the angles. It is also worth mentioning that the lowest increment in the lattice volume was in case of the $C_{O3c}V_{O3c}$ defected structure while C_i defected structure recorded the highest volume increase.

Table V-3 Lattice parameters for the short-listed defected structures.

Structure	Lattice Parameters						Volume (Å)³
	a (Å)	b (Å)	c (Å)	α (°)	β (°)	γ (°)	
m-ZrO_2	10.49	5.22	5.41	90.00	99.27	90.00	292.00
(i) C_{O3c}	10.61	5.25	5.42	89.35	100.01	90.98	297.03
(iii) C_{O3c}-C_{O3c}	10.66	5.28	5.35	91.66	98.68	92.30	297.17
(iv) C_{O3c}=O_{3c}	10.57	5.28	5.39	89.19	98.12	89.92	297.65
(v) C_i	10.89	5.26	5.50	87.64	101.48	92.29	308.39
(x) $C_{O3c}V_{O3c}$	10.50	5.29	5.31	87.72	94.71	90.27	293.68
(xii) C_iV_{O4c}	10.38	5.27	5.50	88.72	98.11	90.65	297.26

5.2 Electronic properties

Analysing the atomic orbitals quantitatively and qualitatively is instrumental for deep understanding of electronic structure that fully dictates electronic properties of pristine and defected m-ZrO_2. In this endeavour, the partial density of states (PDOS) shown in **Figure V-2** as well as the charge populations and population ionicity index (P_i) expressed in **eq. V-1** [161] would be probed to explore the entity of the defect states and the nature of the bonding environment of the studied defective structures as illustrated in **Table V-4**. Additionally, light would be shed on the role and the effect of defect states in modifying bandgap and the effective masses of the charge carriers for the short-listed defective structures as tabulated in **Table V-5**. Also, to pursue the intricate criteria of photoelectrodes, the band edges alignment would be examined against the RHE potential as depicted in **Figure V-3**.

$$P_i = 1 - e^{-\left|\frac{P_C - P}{P}\right|} \qquad \textbf{(V-1)}$$

where P, and P_C are the bond population according to Mulliken charge population and the bond population of pure covalent bond (P_c =1), respectively. P_i ranges between 0 and 1 representing pure covalent and pure ionic bonds, respectively. Upon analysing the PDOS and electronic band structure, it was found that the incorporation of carbon atoms within the m-ZrO_2 crystal (E_g =

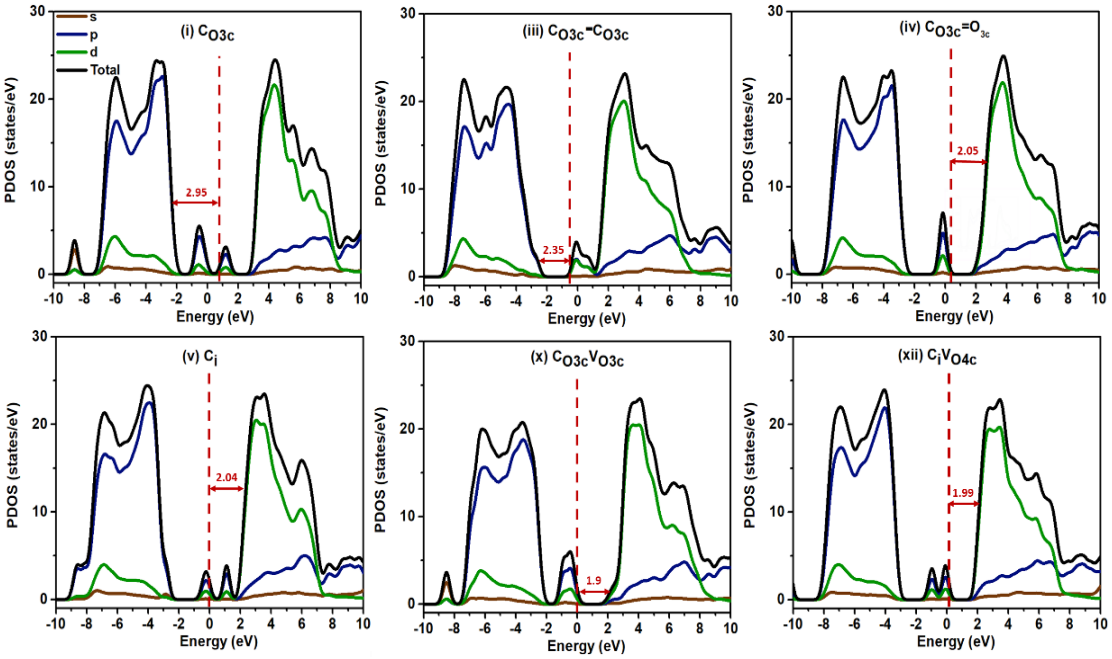

Figure V-2 Partial density of states for the short-listed m-ZrO_2 defective structures.

5.14 eV) introduced intermediate band(s) that resulted in emergence of new bandgap(s) along with the original bandgap (VBM to CBM). Importantly, with the aid of Tauc analysis of optical absorption coefficients of the studied structures, the dominant optical transition was identified to define the dominant new bandgap. Herein, the dominant new bandgap would be endorsed as the bandgap for the upcoming analysis and discussion; since the emerging new bandgap is more favourable for solar energy absorption than original bandgap. In case of (i) and (iii), the carbon defects initiated intermediate sub-conduction band while the rest cases, the carbon defects initiated intermediate sub-valence band. Moreover, in case of (i) and (V), intermediate defect bands laid amid of the new bandgap which act as deep localized defect states (trap states) that causes the increase of recombination rate of charge carriers. By inspection of **Figure V-2**, (iv), (v), (x), and (xii) defective structures gave excellent reduction in bandgap down to nearly 2 eV. On the other hand, (i) and (iii) offered mild bandgap minimization to reach 2.95 and 2.35 eV, respectively. From the analysis of PDOS in **Figure V-2** and the data in **Table V-4**, it was noticed that in (i), (v), and (xii), the defect states are splitted; this may be attributed to the variation of the bonding environment around p_x, p_y and p_z orbitals of the defect species that led to degeneracy breakage. In contrast to the latter case, the defect states in (iii) and (x) showed broadened peaks that can be explained in light of the covalent bonds formed between the two carbon atoms in (iii) and the increased covalency nature in (x) between carbon and the neighbouring zirconium atoms. The left shift of the defect states in (x) and the right shift in (iii) can be credited to the availability of electrons. So, in (x) carbon atom is associated with a vacancy that has dangling bonds with extra electrons that can be invested by the carbon atom in establishing new bonds with the surrounding atoms which is reflected in the bond population in **Table V-4**. Consequently, this causes the stabilization of carbon orbitals accompanied by the decrease in their energies (left shift), on the contrary of (iii) where carbon atom is bonded with another carbon atom that has the same electronegativity (unlike (x)); depriving each other from drawing enough electrons - for bonding - from the host crystal since the available electrons are distributed among them in contrast to (x) as illustrated in their atomic charges in **Table V-4**.

This rendered the carbon orbitals in (iii) less stable causing the right shift in the PDOS compared to (x). Concerning (iv), the established partial-ionic bond between carbon and oxygen atoms induced polarization that slightly incremented the density of the first peak and merged the second defect peak in (i) into the conduction band causing the reduction of the bandgap to 2.05 eV. Regarding (v), the interstitial carbon experienced high repulsive forces due to the congested atomic environment that can be reflected in the fact that it had the highest formation energy in O-poor conditions as presented in **Table V-1**. Therefore, in (xii) the presence of a vacancy nearby the interstitial carbon relieved the repulsive forces experienced by the carbon orbitals; causing the minimization of the separation between the two defect states relative to (v). Similar to (x), the dangling bonds in V_{O4c} offered electrons for the carbon atom leading to the left shift of the defect state peaks in comparison with (v) and also increased the electronic occupation of carbon (decreased the atomic charge) from -0.1 to -0.53 a.u.

Table V-4 Atomic charge, bond length, Mulliken population, ionicity index & bandgap for the short-listed defective structures.

Structure	Atomic charge (a.u)	Bond	Bond length (Å)	Bond population (P)	Ionicity index (P_i)	Bandgap (eV)
(i) C_{O3c}	-0.54	C_1 -- Zr_2	2.30	0.29	0.91	2.95 (indirect)
		C_1 -- Zr_3	2.22	0.46	0.69	
		C_1 -- Zr_8	2.22	0.40	0.77	
(iii) C_{O3c}-C_{O3c}	C_1= -0.68 C_2= -0.58	C_1 -- C_2	1.35	1.49	0.28	2.35 (indirect)
		C_1 -- Zr_2	2.27	0.52	0.60	
		C_2 -- Zr_2	2.54	0.25	0.95	
		C_1 -- Zr_5	2.42	0.25	0.95	
		C_2 -- Zr_8	2.30	0.19	0.98	
(iv) C_{O3c}=O_{3c}	O = -0.69 C = -0.56	C_1 -- O_3	1.49	0.46	0.69	2.05 (indirect)
		C_1 -- Zr_2	2.24	0.05	1.00	
		C_1 -- Zr_3	2.16	0.62	0.45	
		C_1 -- Zr_8	2.21	0.47	0.68	
(v) C_i	-0.1	C_1 -- O_5	1.29	0.74	0.30	2.04 (indirect)
		C_1 -- Zr_5	2.41	0.35	0.84	
		C_1 -- Zr_8	2.25	0.37	0.82	

(x) $C_{O3c}V_{O3c}$	-0.92	C_1 -- Zr_2	2.21	0.48	0.66	1.90 (direct)
		C_1 -- Zr_3	2.09	0.61	0.47	
		C_1 -- Zr_5	2.36	0.41	0.76	
		C_1 -- Zr_8	2.22	0.47	0.68	
(xii) C_iV_{O4c}	-0.53	C_1 -- O_5	1.48	0.49	0.65	1.99 (direct)
		C_1 -- Zr_5	2.27	0.44	0.72	
		C_1 -- Zr_7	2.29	0.59	0.50	
		C_1 -- Zr_8	2.19	0.19	0.99	

5.2.1 Band edge position

For photoelectrochemical water splitting applications, it is essential to account for the relative positions of the bands of the semiconductor to the redox potentials of water species (oxygen and hydrogen). Hence, for overall water splitting with no bias, the conduction band minimum (CBM) and the valence band maximum (VBM) of the semiconductor are required to straddle the reduction potential of hydrogen and the oxidation potential of oxygen, respectively. However, satisfying a part of the aforementioned condition is sufficient to qualify the semiconductor to work as a photoanode if the VBM part is fulfilled while it can serve as a photocathode if the CBM part is fulfilled. With respect to the RHE, the relative displacements between the CBM and the VBM of the short-listed structures were computed given their absolute electronegativities as shown in the following equations [69]:

$$E_{VBM} = \chi - E_e + \frac{1}{2} E_g \qquad \text{(V-2)}$$

$$E_{CBM} = E_{VBM} - E_g \qquad \text{(V-3)}$$

where E_{VBM} and E_{CBM} represent the VBM and CBM potentials, respectively, χ represents the absolute electronegativity of a given structure and it is evaluated through the calculation of the geometric mean of the electronegativities of the isolated constituting atoms of a given structure, and E_e (4.5 eV) represents the energy of free electrons according to the hydrogen scale. The band edge dispositions for the short-listed m-ZrO_2 defective structures is depicted in **Figure V-3** against the redox potentials for water species. From the figure, it is clear that all of the defective structures can work as photoanodes however, (x) $C_{O3c}V_{O3c}$ is the best candidate as it has the lowest bandgap (1.9 eV). It is also important to clarify that (i) C_{O3c} is the only defective structure that straddles the redox potentials of both water species; thus, it can theoretically serve as both photoanode and photocathode undergoing overall water splitting.

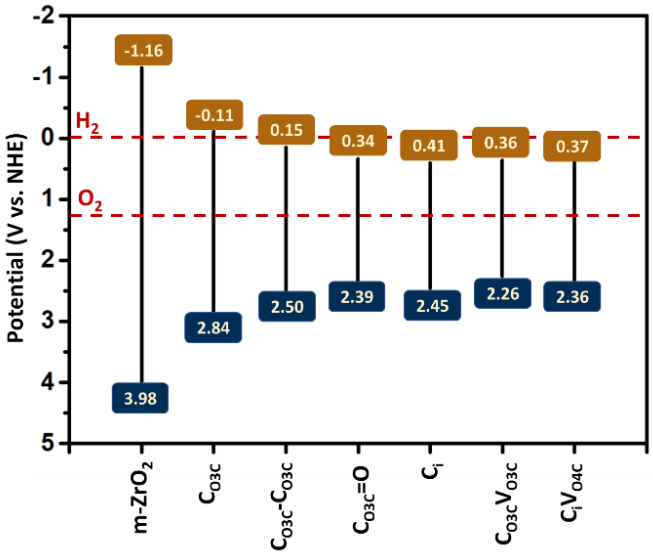

Figure V-3 Band edge dispositions for the short-listed m-ZrO2 defective structures relative to the redox potentials for water species.

5.2.2 Effective mass and exciton binding energy

The photocatalytic activity relies upon the readiness of the electron-hole pair (exciton) generation. In this regard, the effective mass (m^*) of the photogenerated charge carriers is substantial; as it describes the easiness of the motion of the photogenerated carrier within the

semiconductor crystal relative to the mass of free electron as specified in **eq. (V-4)** [69]. Also, the exciton binding energy (E_{ex} in eV) is significant; since it quantifies the energy needed to dissociate an electron-hole pair at its lowest energy state as formulated in **eq. (V-5)** [162].

$$m^* = \pm \hbar^2 \left(\frac{d^2 E_k}{dk^2}\right)^{-1} \qquad \text{(V-4)}$$

$$E_{ex} \approx 13.56 \frac{m^\dagger}{m_e \varepsilon} \qquad \text{(V-5)}$$

where m_h^* and m_e^* (kg) represent the effective masses of holes and electrons; respectively, ħ represents reduced Planck's constant, E_k represents the energy corresponding to the wave vector k, $m^\dagger$represents the reduced effective mass of the exciton ($1/m^\dagger = 1/m_h^* + 1/m_e^*$), m_e is the rest mass of an electron, and ε is the dielectric constant. D in **Table V-5** represents the ratio between m_e^* and m_h^* and it reflects the charge recombination rate. To this end, a large difference is required between the effective masses of the photogenerated electrons and holes to secure the spatial separation between them ensuring low charge carrier recombination rates [163], thus enhancing the photocatalytic efficiency. For the short-listed structures, (iii), (x), and (xii) gave the best D values indicating low recombination rates. However, (x) $C_{O3c}V_{O3c}$ demonstrated the lowest m_e^*; resulting in high mobility and fast charge transfer in comparison to all studied structures including m-ZrO_2. For efficient dissociation of excitons at room temperature, E_{ex} is necessary to be lower than k_BT ~25 meV [164]. (x) $C_{O3c}V_{O3c}$ provided the highest reduction in E_{ex} (91 meV) relative to m-ZrO_2 (169 meV). Even though 91 meV is greater than the required E_{ex} (25 meV), the DFT calculations were employed at 0 K thus, the required E_{ex} is predicted to be lower than 91 meV and probably lower than 25 meV at room temperature.

Table V-5 Effective masses and exciton binding energy for the photogenerated charge carriers of the short-listed defective structures.

Structure		m_h^*/m_e		m_e^*/m_e		**D**	**E_{ex} (meV)**
m-ZrO_2	**Direction**	*G→F*	*G→Z*	*G→F*	*G→Z*	2.72	169
	Calculation	0.33	0.25	0.38	1.20		

	Average	0.29		0.79			
(i) C_{O3c}	**Direction**	*G→F*	*G→Z*	*Z→Q*	*Z→G*	2.69	179
	Calculation	0.42	0.32	1.77	0.22		
	Average	0.37		1.00			
(iii) C_{O3c}-C_{O3c}	**Direction**	*G→F*	*G→Z*	*Z→Q*	*Z→G*	9.56	655
	Calculation	0.2	2.97	29.72	0.59		
	Average	1.59		15.16			
(iv) C_{O3c}=O_{3c}	**Direction**	*G→F*	*G→Z*	*Z→Q*	*Z→G*	0.32	176
	Calculation	1.22	1.25	0.50	0.28		
	Average	1.24		0.39			
(v) C_i	**Direction**	*Z→Q*	*Z→G*	*G→F*	*G→Z*	1.09	240
	Calculation	0.25	1.14	0.52	0.99		
	Average	0.70		0.76			
(x) $C_{O3c}V_{O3c}$	**Direction**	*G→F*	*G→Z*	*G→F*	*G→Z*	0.22	91
	Calculation	0.33	1.46	0.24	0.16		
	Average	0.90		0.20			
(xii) C_iV_{O4c}	**Direction**	*G→F*	*G→Z*	*Q→F*	*Q→Z*	6.01	521
	Calculation	1.39	0.87	11.89	1.70		
	Average	1.13		6.80			

5.3 Optical properties

Investigation of optical properties for candidate materials of electrodes for photoelectrochemical water splitting is a paramount decisive step for such an intricate optoelectronic application.

5.3.1 Dielectric function and dielectric constant

The complex dielectric function $\varepsilon(\omega)$ is the most fundamental function in optics on which all the other optical properties are dependent as expressed in the methods section (Chapter IV). By inspection of the optical properties in **Figure V-4 (a,b)** and **V-5**, it is unequivocal that m-ZrO_2 and the short-listed defected structures reveal almost perfect isotropic behaviour in the dielectric function along the three spatial dimensions. From the real part of the dielectric function, the static dielectric constant $\varepsilon_1(0)$ defines the permittivity of the material that is favourable to be high for solar water splitting purposes as this may lead to lowering E_{ex}; leading to improved charge carrier extraction efficiency. All the short-listed defective structures possess slightly higher $\varepsilon_1(0)$ values (4.52-5.45 F/m) than m-ZrO_2 (4.13 F/m). For the imaginary part of the dielectric function $\varepsilon_2(\omega)$, $\varepsilon_2(0)$ reflects light-matter interaction between the incident photons and electrons which in turn elaborate the light absorption capability. In our case, all the structures showed no improvement in $\varepsilon_2(0)$ in comparison with the pristine case. Moreover, the main peaks in $\varepsilon_2(\omega)$ shown in **Figure V-4** and **V-5** indicate the possible electronic transitions across the main and intermediate bands, so coupling the analysis of $\varepsilon_2(\omega)$ with the absorption function $\alpha(\omega)$ provides sharper insights.

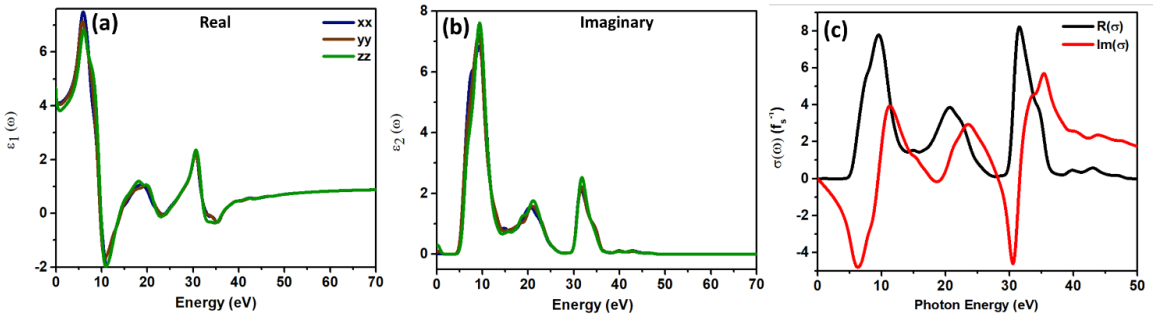

Figure V-4 Optical properties of m-ZrO2 (a-b) The real and imaginary parts of the diagonal components of the dielectric constants of the defected structures respectively, and (b) optical conductivity.

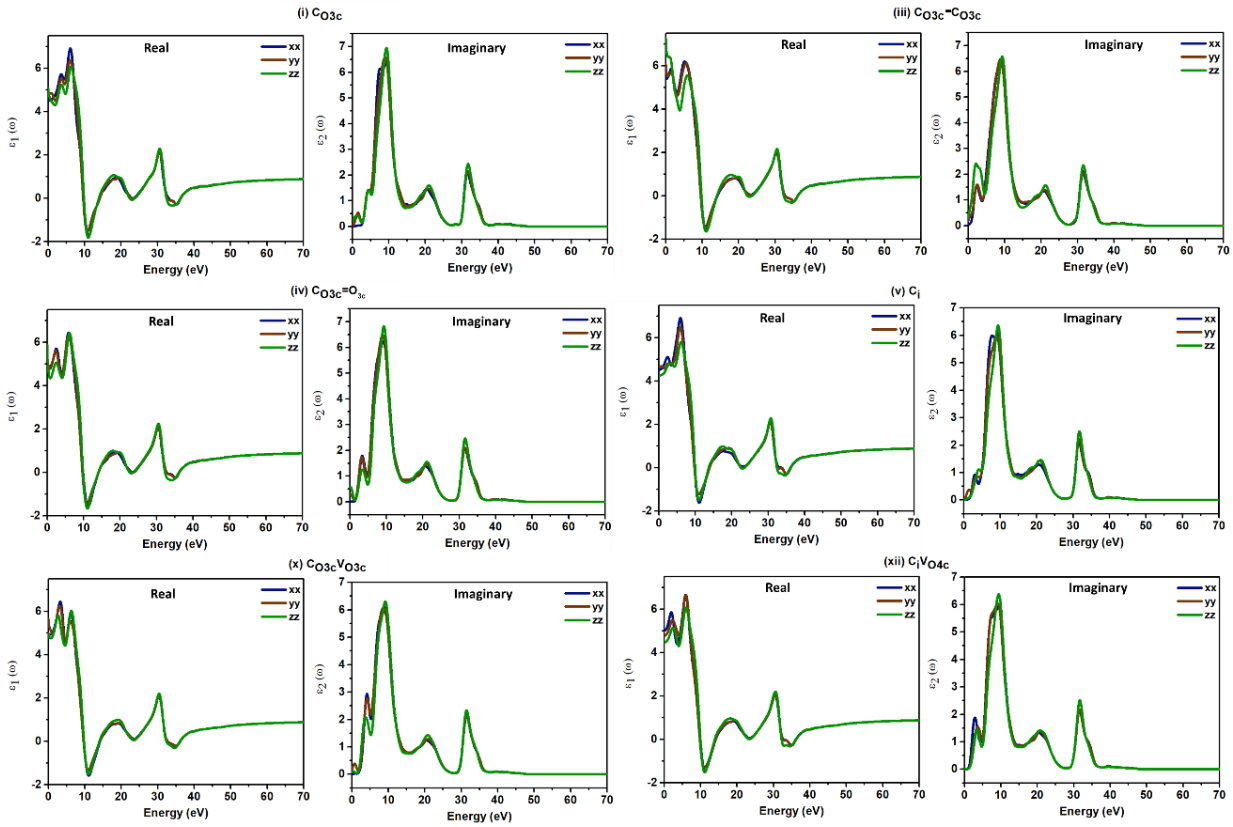

Figure V-5 The real and imaginary parts of the diagonal components of the dielectric constants of the defected structures.

5.3.2 Absorption coefficient

All the defective structures enhanced the light absorption with different degrees due to introduction of intermediate bands with different positions within m-ZrO_2 bandgap. As

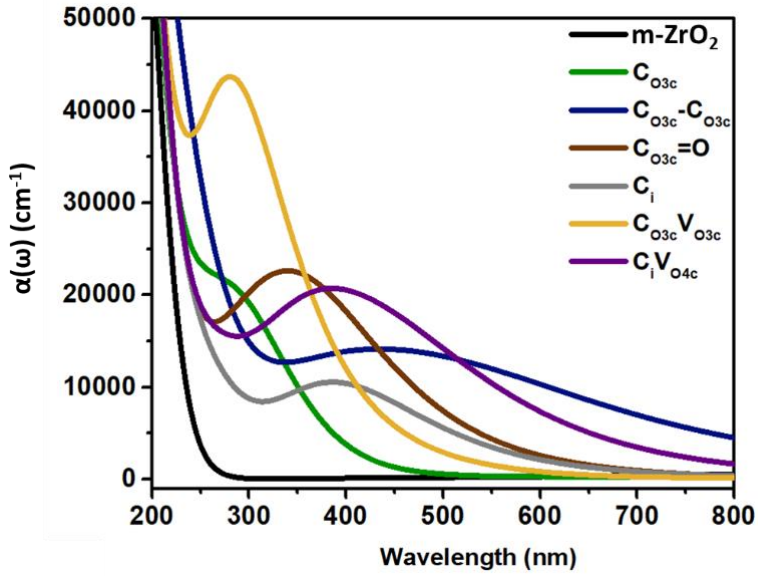

Figure V-6 Absorption coefficient of the short-listed defective structures and m-ZrO_2.

displayed in **Figure V-4** and **V-5**, the $\varepsilon_2(\omega)$ of the defective structures manifested the presence of peaks within the range of 0-9.5 eV ((x) $C_{O3c}V_{O3c}$ offered the highest peak) substantiating the evidence of enhanced absorption and the existence of more electronic transitions relative to pristine case which lacked any peaks in the aforementioned range. To this end, the intermediate bands minimized the bandgap; allowing for more incident photons of less energy within the visible region to get absorbed by the material contributing in the photogeneration of charge carriers. As shown in **Figure V-6**, $\alpha(\omega)$ of m-ZrO_2 vanishes near 300 nm (ultra-violet region) while the defective structures sustained the absorption within the visible region.

5.3.3 Optical conductivity

The real $R(\sigma)$ and imaginary $Im(\sigma)$ parts of the optical conductivity represent the in-phase current and out-phase inductive currents, respectively. The in-phase current is usually accompanied by liberation of heat energy due to the resistance [148]. In **Figure V-4 (c)** and **V-7**, the in-phase current dominates over the range 0-34.5 eV (resistance domain) then, the out-phase current takes over after 34.5 eV (induction domain) at which neither energy from the electric field is absorbed nor liberation of heat from the crystal occurs. In the region of 0-5 eV of **Figure V-4 (c)** and **V-7**, peaks in both real and imaginary parts exist whose positions are consistent with the new emergent bandgaps for each defective structure.

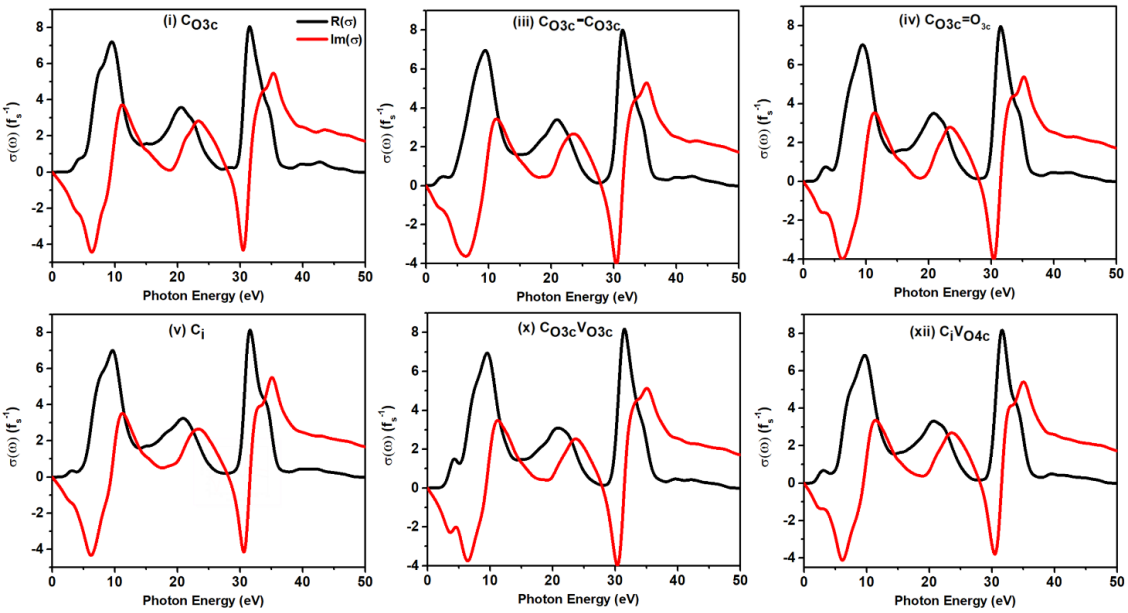

Figure V-7 Optical conductivity σ(ω) of the defected structures.

5.3.4 Optical reflectivity

The reflectivity spectrum *R(ω)* in **Figure V-8 (a)** exhibits three peaks at 12, 24, and 36 eV. With the aid of PDOS, the lowest frequency peak signifies the interband transition between the hybridized states within the conduction band while the highest peak indicates the band-to-band transition from the VBM states to the CBM states. Furthermore, the reflectivity at infinite length *R(0)* is around 0.15 whereas the reflectivity dies out for frequencies more than 50 eV. It is noteworthy that (x) $C_{O3c}V_{O3c}$ offered the lowest average reflectivity.

5.3.5 Energy loss function

The energy loss function $L(\omega)$ quantifies the energy lost due to a fast-traversing electron within the material. In the $L(\omega)$ spectrum in **Figure V-8 (b)**, the peaks at 14.3, 24.5, and 36.5 eV indicates the characteristic plasma frequencies rather than being interband

electronic transitions because $\varepsilon_1(\omega)$ at each peak is equal to zero confirming the occurrence of plasma oscillations [165].

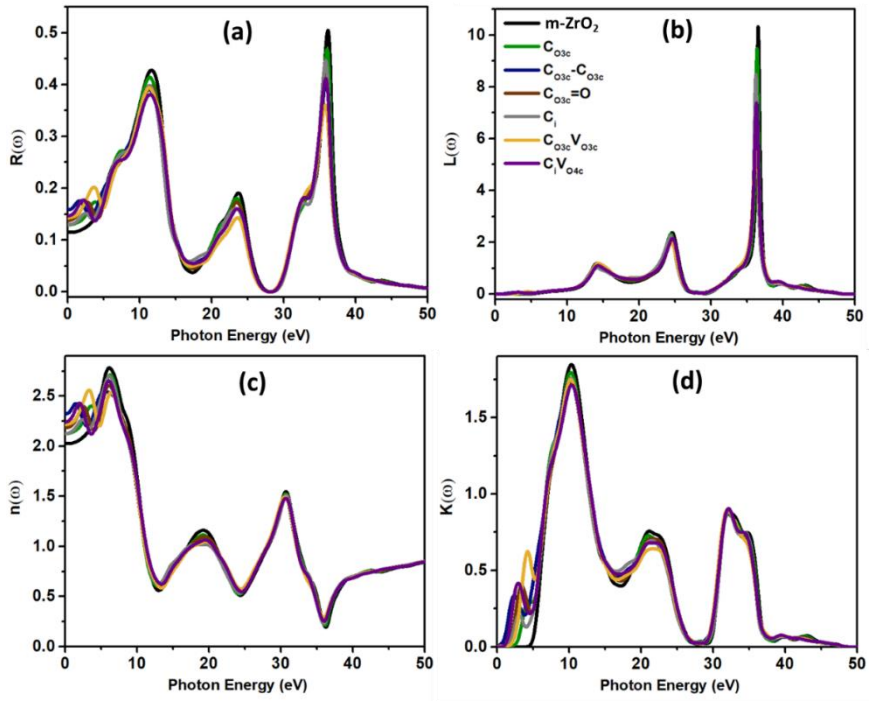

Figure V-8 Calculated optical properties of the defected structures (a) reflectivity R(ω), (b) energy loss function L(ω), (c) refractive index n(ω), and (d) extinction coefficient K(ω).

5.3.6 Refractive index and extinction coefficients

The refractive index in **Figure V-8 (c)** demonstrates nearly the same three peaks at 6.3, 19.2, 30.6 eV while a peak for each defective structure is present within the 0-5 eV range attributed to the various intermediate band positions of the defective structures within the m-ZrO_2 bandgap. The static refractive index $n(0)$ is in the range of 2-2.3 for all the defective structures and m-ZrO_2. The extinction coefficient $k(\omega)$ describes the absorption loss upon the propagation of an electromagnetic wave through the material. In **Figure V-8 (d)**, $k(\omega)$ exhibits three peaks at 10.15, 21.5, and 32.1 eV. For low energy photons, $k(\omega)$ has zero values within the range of the bandgap of each structure. For instance, $k(\omega)$ remains zero from 0- 5 eV which is nearly the bandgap of pristine m-ZrO_2. Also, for each defective structure, there is a peak before 5 eV marking the intermediate band position within the bandgap of m-ZrO_2.

Chapter VI : Quantum Capacitance Calculation for Carbon-Based Supercapacitors

DFT was used to study the quantum capacitance in different carbon allotropes. As shown in **Figure VI-1 (a)**, the DOS of CNTs, GNP, and Gr are centred around zero with the DOS of CNT > GR ~ GNP. The gravimetric quantum capacitance is presented in **Figure VI-1 (b)** in the potential window between -1 to 1V, which is the maximum attained potential window experimentally. While CNTs showed the highest C_Q in both positive and negative potential windows, both GNP and Gr showed almost the same C_Q. The high quantum capacitance of graphite was expected as DFT assumed that all the bulk material will contribute to the quantum capacitance. However, assuming that only the surface layers of graphite will contribute to the quantum capacitance, it can be estimated that the C_Q of graphene is higher than that of graphite. For the values of the quantum capacitance, it can be observed that both graphene and graphite are giving V-shaped curves around the point of zero charge, in agreement with the literature [131,134]. However, CNTs showed a semi V-shape due to the unsymmetrical DOS around the Fermi-level [108]. The V-shape curve gives insights on the reason behind the increased capacitance with increasing the potential window range. However, in the experimental work, CNTs showed a maximum capacitance in the positive potential window of 1377 F/g and 477 F/g in the negative potential window. In the negative potential window, the experimental EDL was the leading charge storage mechanism, which made use of the quantum capacitance. The calculated C_Q explains the experimentally obtained higher capacitance of CNTs in the positive potential window than in the negative potential window and the higher capacitance than both GNP and Gr. For the GNP and Gr, the symmetrical V-shaped C_Q curve explains the almost equal capacitance values as positive and negative electrodes.

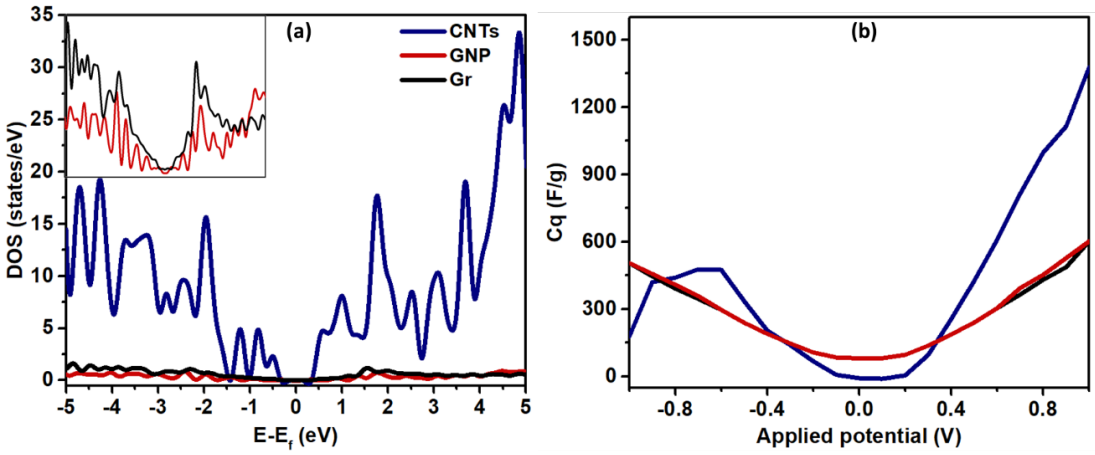

Figure VI-1: Computational investigation of the carbon tested materials. (a) DOS of the studied carbon materials (inset: enlargement of the DOS of the GNP and Gr), and (b) the calculated quantum capacitance of the studied carbon materials.

Since doping the carbon materials have been one of the leading methods to improve the capacitance performance, the DFT was used to unveil the secret behind the enhanced capacitance. The high performance of the nitrogen-doped graphene (NDG), A unit cell with N-doped graphene was simulated using DFT. The cell included graphitic nitrogen, pyridinic nitrogen, and pyrrolic nitrogen. The results were compared to the pristine graphene. The bond distance between the N-Pyrrolic and the adjacent bonded carbon was 1.43 Å, while the bond distance between the N-Pyrrolic and the adjacent non-bonded carbon was 2.26 Å. For the N-Graphitic-C bond distance, it was ~1.39 Å, while It was 1.44 Å for the N-Pyridinic with the adjacent non-bonded carbon. The total density of states (TDOS) of the simulated NDG was calculated as presented in **Figure V-2 (a)**, the TDOS was compared to that of the pristine graphene (G). It can be observed that the TDOS of the NDG was much higher than that of the G and that the bandgap was reduced dramatically from 0.44 eV for G to 0.09 eV for the NDG. This may be attributed to the effect of the free electrons on the nitrogen atoms. Although it was reported that the N-doping increases the quantum capacitance (C_Q) of the graphene [133,153], a mixture of different nitrogen defects types was not yet reported. The C_Q presented in **Figure V-2 (b)**, shows that the mixed N-doping increased the C_Q dramatically. The highest graphene C_Q calculated was 792 F/g for G while it was 2440 F/g for NDG. The experimental values usually are lower than the reported C_Q due to the resistance from the electrolyte and from the other

circuit parameters. Besides the electrode/electrolyte interaction directed by the diffusion-controlled process can lead to reduction in the total capacitance. However, the C_Q can give a great insight on the origin of the total high capacitance resulted and the trend of increment of capacitance. To this end, it can be concluded that the N-doping with mixed graphitic, pyrrolic and pyridinic can give a high impact on the capacitance performance of the electrode material.

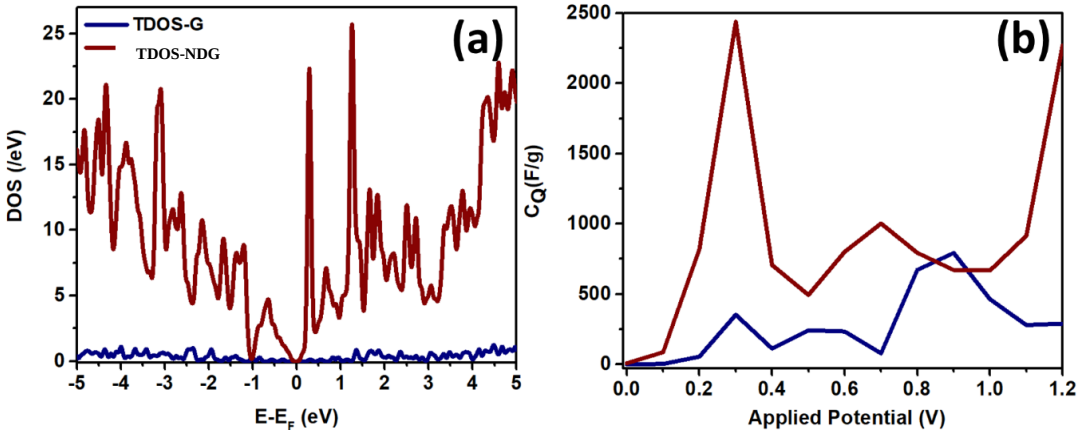

Figure VI-2 Calculated electronic properties (a) DOS of graphene and NDG, and (b) Quantum capacitance of graphene and NDG.

Chapter VII : Conclusions

In pursuance of the holy-grail overall water splitting, the materials community is striving to design and tune novel efficient electrode materials to uphold this endeavour. In this study, the first-principles calculations embodied in DFT was employed to investigate the thermodynamic, electronic, and optical properties of various carbon doping scenarios in m-ZrO_2. The defect formation energies (E_D^f) revealed that elevating the temperature promotes and facilitates the formation of carbon defects. Moreover, it was observed that $C_{O3c}V_{O3c}$, and $C_i\,V_{O4c}$ had the lowest formation energy. Concerning the binding energies (E_b), all the complex defects were confirmed to be stable. The analysis of the electronic structure coupled with the absorption coefficient defined the new emerging bandgaps where $C_{O3c}V_{O3c}$ showed the narrowest bandgap (1.9 eV). Furthermore, the band edge positions against the redox potentials of water species elucidated that all the studied defective structures can serve as photoanode. Albeit, $C_{O3c}V_{O3c}$ being the best. It is noteworthy that C_{O3c} was the only defective structure that exhibited the slight straddling of the redox potentials of water species. Upon examining the exciton binding energy (E_{ex}), it was noticed that $C_{O3c}V_{O3c}$ possessed the least E_{ex}. By the assessment of charge carrier recombination rate via computing the ratio between m_e^* and m_h^*denoted by D, C_{O3c}-C_{O3c}, $C_{O3c}V_{O3c}$, and C_iV_{O4c} demonstrated the least recombination rate. It is worth mentioning that $C_{O3c}V_{O3c}$ had the lowest m_e^* which implies high mobility and fast charge transfer. The optical properties including dielectric function, absorption coefficient, conductivity, reflectivity, energy loss function, refractive index, and extinction coefficients were studied for the defective structures along with m-ZrO_2. Importantly, all the defective structures enhanced the light absorption to different extents. Through the analysis of optical properties, with the exception of the absorption coefficients, the optical properties of the m-ZrO_2 and the short-listed defective structures nearly share the same trend with slight

variations associated with the different positions of the intermediate bands and new emerging bandgaps for each structure. Nonetheless, $C_{O3c}V_{O3c}$ offered the highest static dielectric constant $\varepsilon_1(0)$, the lowest average reflectivity as well as enhanced light absorption. Thereby, this study highly recommends $C_{O3c}V_{O3c}$ defected m-ZrO_2 to be pushed forward for experimental test-bed validations as a photoanode material of tremendous potential for PEC water splitting applications.

DFT proved to be a good tool to predict the capacitance behaviour of carbon electrodes. The calculations of the C_Q revealed the reason behind the high capacitance of the CNTs over the GNP and the Gr and also gave insights on the origin of the higher positive potential window capacitance of the CNTs. While the GNP and Gr gave almost equal experimental capacitance in the positive and negative potential values due to the symmetrical V-shaped C_Q curve. Also, the DFT study shed the light on the quantum capacitance enhancement resulted upon doping the graphene with graphitic, pyrrolic, and pyridinic nitrogen together. The C_Q calculation via DFT proved that doping graphene with multi-dopants can give a great impact on the DOS and hence the overall EDL performance of the electrode. Moreover, future work can target the use of DFT to study variant dopants atoms with different ratios prior to the synthesis method which will decrease money, time, and efforts.

This study actively contributes to the advancement of the hierarchical materials data-bases towards the novel efficient data-driven materials design approach.

References

1. Kalidindi, S. R. *Hierarchical Materials Informatics: Novel Analytics for Materials Data*. *Hierarchical Materials Informatics: Novel Analytics for Materials Data* (2015). doi:10.1016/C2012-0-07337-1.

2. Kreculj, D. & Rasuo, B. Impact damage modelling in laminated composite aircraft structures. in *Sustainable Composites for Aerospace Applications* 125–153 (Elsevier, 2018). doi:10.1016/B978-0-08-102131-6.00007-4.

3. Hellman, A. & Wang, B. First-principles view on photoelectrochemistry: Water-splitting as case study. *Inorganics* vol. 5 37 (2017).

4. Gameel, K. M., Sharafeldin, I. M., Abourayya, A. U., Biby, A. H. & Allam, N. K. Unveiling CO adsorption on Cu surfaces: New insights from molecular orbital principles. *Phys. Chem. Chem. Phys.* **20**, 25892–25900 (2018).

5. Hamza, M. A., El-Shazly, A. N., Tolba, S. A. & Allam, N. K. Novel Bi-based photocatalysts with unprecedented visible light-driven hydrogen production rate: Experimental and DFT insights. *Chem. Eng. J.* **384**, 123351 (2020).

6. Ali, B. A., Biby, A. H. & Allam, N. K. Fullerene C_{76}: An Unexplored Superior Electrode Material with Wide Operating Potential Window for High-Performance Supercapacitors. *ChemElectroChem* **7**, 1672–1678 (2020).

7. Ali, B. A. & Allam, N. K. A first-principles roadmap and limits to design efficient supercapacitor electrode materials. *Physical Chemistry Chemical Physics* vol. 21 17494–17511 (2019).

8. Hasan, M. M., Tolba, S. A. & Allam, N. K. In Situ Formation of Graphene Stabilizes Zero-Valent Copper Nanoparticles and Significantly Enhances the Efficiency of Photocatalytic Water Splitting. *ACS Sustain. Chem. Eng.* **6**, 16876–16885 (2018).

9. Sharma, G. *et al.* Electronic structure, photovoltage, and photocatalytic hydrogen evolution with p-CuBi 2 O 4 nanocrystals †. (2016) doi:10.1039/c5ta07040f.

10. Huda, M. N., Deutsch, T. G., Sarker, P. & Turner, J. A. Electronic structure study of N, O related defects in GaP for photoelectrochemical applications. *J. Mater. Chem. A* **1**, 8425–8431 (2013).

11. Pilania, G. *et al.* Machine learning bandgaps of double perovskites. *Sci. Rep.* **6**, (2016).

12. Curtarolo, S. *et al.* The high-throughput highway to computational materials design. *Nat. Mater.* **12**, 191–201 (2013).

13. Smil, V. *Energy and civilization : a history*.

14. Di Muzio, T. *Carbon capitalism : energy, social reproduction and world order*.

15. Meadows, D. H., Randers, J. & Meadows, D. L. *The limits to growth : the 30-year update*.

16. Anco S. Blazev. *Energy Security for The 21st Century*. (2015).

17. Schumacher, D. & Schumacher, D. The 1973 Oil Crisis and its Aftermath. in *Energy: Crisis or Opportunity?* 21–41 (Macmillan Education UK, 1985). doi:10.1007/978-1-349-17797-4_2.

18. Spellman, F. R. *Environmental impacts of renewable energy*.

19. Kim, J. H., Hansora, D., Sharma, P., Jang, J. W. & Lee, J. S. Toward practical solar hydrogen production-an artificial photosynthetic leaf-to-farm challenge. *Chem. Soc. Rev.* **48**, 1908–1971 (2019).

20. Nowotny, J., Sorrell, C. C., Bak, T. & Sheppard, L. R. Solar-hydrogen: Unresolved problems in solid-state science. *Sol. Energy* **78**, 593–602.

21. Sahaym M Grant Norton, U. A. Advances in the application of nanotechnology in enabling a 'hydrogen economy'. doi:10.1007/s10853-008-2749-0.

22. solar energy | Description, Uses, & Facts | Britannica. https://www.britannica.com/science/solar-energy.

23. FUJISHIMA, A. & HONDA, K. Electrochemical Photolysis of Water at a Semiconductor Electrode. *Nature* **238**, 37–38 (1972).

24. Ahmed, M. & Dincer, I. A review on photoelectrochemical hydrogen production systems: Challenges and future directions. *Int. J. Hydrogen Energy* **44**, 2474–2507 (2019).

25. Jiang, C., Moniz, S. J. A., Wang, A., Zhang, T. & Tang, J. Photoelectrochemical devices for solar water splitting-materials and challenges. *Chem. Soc. Rev.* **46**, 4645–4660 (2017).

26. Yang, Y. *et al.* Progress in Developing Metal Oxide Nanomaterials for Photoelectrochemical Water Splitting. *Adv. Energy Mater.* **7**, 1–26 (2017).

27. Li, X. *et al.* Photoelectrochemical properties of CdSe quantum dot sensitized p-type flower-like NiO solar cells with different deposition layer. *Mater. Res. Bull.* **84**, 212–217 (2016).

28. Pan, H. Principles on design and fabrication of nanomaterials as photocatalysts for water-splitting. *Renewable and Sustainable Energy Reviews* vol. 57 584–601 (2016).

29. Hisatomi, T., Kubota, J. & Domen, K. Recent advances in semiconductors for photocatalytic and photoelectrochemical water splitting. *Chem. Soc. Rev.* **43**, 7520–7535 (2014).

30. Zhang, Y. *et al.* Doping-promoted solar water oxidation on hematite photoanodes. *Molecules* vol. 21 (2016).

31. Jafari, T. *et al.* Photocatalytic water splitting - The untamed dream: A review of recent advances. *Molecules* vol. 21 (2016).

32. Gupta, N. M. Factors affecting the efficiency of a water splitting photocatalyst: A perspective. *Renewable and Sustainable Energy Reviews* vol. 71 585–601 (2017).

33. Moon, S. Y., Gwag, E. H. & Park, J. Y. Hydrogen Generation on Metal/Mesoporous Oxides: The Effects of Hierarchical Structure, Doping, and Co-catalysts. *Energy Technology* vol. 6 459–469 (2018).

34. Zhang, G., Liu, G., Wang, L. & Irvine, J. T. S. Inorganic perovskite photocatalysts for solar energy utilization. *Chemical Society Reviews* vol. 45 5951–5984 (2016).

35. Wang, G., Yang, Y., Han, D. & Li, Y. Oxygen defective metal oxides for energy conversion and storage. *Nano Today* vol. 13 23–39 (2017).

36. Kim, J. H. & Lee, J. S. Elaborately Modified BiVO4 Photoanodes for Solar Water Splitting. *Advanced Materials* vol. 31 (2019).

37. Haque, F., Daeneke, T., Kalantar-zadeh, K. & Ou, J. Z. Two-Dimensional Transition Metal Oxide and Chalcogenide-Based Photocatalysts. *Nano-Micro Letters* vol. 10 (2018).

38. Di Valentin, C., Pacchioni, G. & Selloni, A. Theory of carbon doping of titanium dioxide. *Chem. Mater.* **17**, 6656–6665 (2005).

39. Wang, H. & Lewis, J. P. Effects of dopant states on photoactivity in carbon-doped TiO2. *J. Phys. Condens. Matter* **17**, (2005).

40. Park, J. H., Kim, S. & Bard, A. J. Novel carbon-doped TiO 2 nanotube arrays with high aspect ratios for efficient solar water splitting. *Nano Lett.* **6**, 24–28 (2006).

41. Wu, G., Nishikawa, T., Ohtani, B. & Chen, A. Synthesis and characterization of carbon-doped TiO2 nanostructures with enhanced visible light response. *Chem. Mater.* **19**, 4530–4537 (2007).

42. Kesong, Y., Ying, D., Baibiao, H. & Myung-Hwan, W. Density functional

characterization of the visible-light absorption in substitutional C-anion- and C-cation-doped TiO 2. *J. Phys. Chem. C* **113**, 2624–2629 (2009).

43. Lu, J. *et al.* Chemical and optical properties of carbon-doped TiO 2: A density-functional study. *Appl. Phys. Lett.* **100**, (2012).

44. Sun, Y. Y. & Zhang, S. Kinetics stabilized doping: computational optimization of carbon-doped anatase TiO2 for visible-light driven water splitting. *Phys. Chem. Chem. Phys.* **18**, 2776–2783 (2016).

45. Ricca, C., Ringuedé, A., Cassir, M., Adamo, C. & Labat, F. A comprehensive DFT investigation of bulk and low-index surfaces of ZrO2 polymorphs. *J. Comput. Chem.* **36**, 9–21 (2015).

46. Asle Zaeem, M., Zhang, N. & Mamivand, M. A review of computational modelling techniques in study and design of shape memory ceramics. *Comput. Mater. Sci.* **160**, 120–136 (2019).

47. Ebbesen, S. D., Jensen, S. H., Hauch, A. & Mogensen, M. B. High temperature electrolysis in alkaline cells, solid proton conducting cells, and solid oxide cells. *Chem. Rev.* **114**, 10697–10734 (2014).

48. Aryanfar, A. *et al.* Integrated Computational Modelling of Water Side Corrosion in Zirconium Metal Clad Under Nominal LWR Operating Conditions. *Jom* **68**, 2900–2911 (2016).

49. Sun, C., Hui, R., Qu, W. & Yick, S. Progress in corrosion resistant materials for supercritical water reactors. *Corros. Sci.* **51**, 2508–2523 (2009).

50. Zhang, J., Li, L., Zhang, J., Zhang, X. & Zhang, W. Controllable design of natural gully-like TiO2-ZrO2 composites and their photocatalytic degradation and hydrogen production by water splitting. *New J. Chem.* **41**, 9113–9122 (2017).

51. Reddy, V. R., Hwang, D. W. & Lee, J. S. Photocatalytic Water Splitting over ZrO2

Prepared by Precipitation Method. *Korean J. Chem. Eng.* **20**, 1026–1029 (2003).

52. Kaneko, H., Taku, S. & Tamaura, Y. Reduction reactivity of CeO2-ZrO2 oxide under high O2 partial pressure in two-step water splitting process. *Sol. Energy* **85**, 2321–2330 (2011).

53. Reddy, C. V. *et al.* Efficient removal of toxic organic dyes and photoelectrochemical properties of iron-doped zirconia nanoparticles. *Chemosphere* **239**, 124766 (2020).

54. Yan, G. X., Wang, A., Wachs, I. E. & Baltrusaitis, J. Critical review on the active site structure of sulfated zirconia catalysts and prospects in fuel production. *Appl. Catal. A Gen.* **572**, 210–225 (2019).

55. Opoku, F., Govender, K. K., van Sittert, C. G. C. E. & Govender, P. P. Enhancing photocatalytic activity for hydrogen production and pollutant degradation by modifying tetragonal ZrO2 with monolayers slab surface of BiVO4, Ag3PO4, SrTiO3 and WO3: A first-principles study. *Comput. Mater. Sci.* **138**, 462–473 (2017).

56. Agorku, E. S., Kuvarega, A. T., Mamba, B. B., Pandey, A. C. & Mishra, A. K. Enhanced visible-light photocatalytic activity of multi-elements-doped ZrO2 for degradation of indigo carmine. *J. Rare Earths* **33**, 498–506 (2015).

57. Onsuratoom, S., Chavadej, S. & Sreethawong, T. Hydrogen production from water splitting under UV light irradiation over Ag-loaded mesoporous-assembled TiO2-ZrO2 mixed oxide nanocrystal photocatalysts. *Int. J. Hydrogen Energy* **36**, 5246–5261 (2011).

58. Yasin, A. S., Mohamed, I. M. A., Park, C. H. & Kim, C. S. Design of novel electrode for capacitive deionization using electrospun composite titania/zirconia nanofibers doped-activated carbon. *Mater. Lett.* **213**, 62–66 (2018).

59. Kim, E. T. & Yoon, S. G. Characterization of zirconium dioxide film formed by plasma enhanced metal-organic chemical vapor deposition. *Thin Solid Films* **227**, 7–12 (1993).

60. Varanasi, V. G. *et al.* High-growth rate YSZ thermal barrier coatings deposited by

MOCVD demonstrate high thermal cycling lifetime. *Mater. Sci. Eng. A* **528**, 978–985 (2011).

61. Mahato, N., Banerjee, A., Gupta, A., Omar, S. & Balani, K. Progress in material selection for solid oxide fuel cell technology: A review. *Prog. Mater. Sci.* **72**, 141–337 (2015).

62. Chen, Y. W., Moussi, J., Drury, J. L. & Wataha, J. C. Zirconia in biomedical applications. *Expert Rev. Med. Devices* **13**, 945–963 (2016).

63. Zhang, Y. & Lawn, B. R. Novel Zirconia Materials in Dentistry. *J. Dent. Res.* **97**, 140–147 (2018).

64. Gokon, N., Yamamoto, H., Kondo, N. & Kodama, T. Internally circulating fluidized bed reactor using m-ZrO2 supported NiFe2O4 particles for thermochemical two-step water splitting. *J. Sol. Energy Eng. Trans. ASME* **132**, 0211021–02110210 (2010).

65. Pezzotti, G. Bioceramics for hip joints: The physical chemistry viewpoint. *Materials (Basel).* **7**, 4367–4410 (2014).

66. Miura, N., Sato, T., Anggraini, S. A., Ikeda, H. & Zhuiykov, S. A review of mixed-potential type zirconia-based gas sensors. *Ionics (Kiel).* **20**, 901–925 (2014).

67. Liu, T., Zhang, X., Wang, X., Yu, J. & Li, L. A review of zirconia-based solid electrolytes. *Ionics (Kiel).* **22**, 2249–2262 (2016).

68. Hernández, S. *et al.* Insights into the sunlight-driven water oxidation by Ce and Er-doped ZrO2. *Front. Chem.* **6**, (2018).

69. Tolba, S. A. & Allam, N. K. Computational Design of Novel Hydrogen-Doped, Oxygen-Deficient Monoclinic Zirconia with Excellent Optical Absorption and Electronic Properties. *Sci. Rep.* **9**, 1–12 (2019).

70. Amer, A. W., El-Sayed, M. A. & Allam, N. K. Tuning the Photoactivity of Zirconia

Nanotubes-Based Photoanodes via Ultrathin Layers of ZrN: An Effective Approach toward Visible-Light Water Splitting. *J. Phys. Chem. C* **120**, 7025–7032 (2016).

71. Zeng, Q. *et al.* Integrated Photorechargeable Energy Storage System: Next-Generation Power Source Driving the Future. *Adv. Energy Mater.* **10**, 1–30 (2020).

72. Lau, D. *et al.* Hybrid solar energy harvesting and storage devices: The promises and challenges. *Mater. Today Energy* **13**, 22–44 (2019).

73. Wang, Y., Song, Y. & Xia, Y. Electrochemical capacitors: mechanism, materials, systems, characterization and applications. *Chem. Soc. Rev.* **45**, 5925–5950 (2016).

74. Ahmed, N., Ali, B. A., Ramadan, M. & Allam, N. K. Three-Dimensional Interconnected Binder-Free Mn–Ni–S Nanosheets for High Performance Asymmetric Supercapacitor Devices with Exceptional Cyclic Stability. *ACS Appl. Energy Mater.* **2**, 3717–3725 (2019).

75. Gogotsi, Y. & Penner, R. M. Energy Storage in Nanomaterials – Capacitive, Pseudocapacitive, or Battery-like? *ACS Nano* **12**, 2081–2083 (2018).

76. Ali, B. A., Metwalli, O. I., Khalil, A. S. G. & Allam, N. K. Unveiling the Effect of the Structure of Carbon Material on the Charge Storage Mechanism in MoS_2 -Based Supercapacitors. *ACS Omega* **3**, 16301–16308 (2018).

77. Zhong, C. *et al.* A review of electrolyte materials and compositions for electrochemical supercapacitors. *Chem. Soc. Rev.* **44**, 7484–7539 (2015).

78. Ali, B. A. & Allam, N. K. Silkworms as a factory of functional wearable energy storage fabrics. *Sci. Rep.* **9**, 1–8 (2019).

79. Ho, K. C. & Lin, L. Y. A review of electrode materials based on core-shell nanostructures for electrochemical supercapacitors. *J. Mater. Chem. A* **7**, 3516–3530 (2019).

80. Ding, J. F. *et al*. Electronic and optical properties of anion-doped c-ZrO2 from first-principles calculations. *J. Cent. South Univ.* **21**, 2584–2589 (2014).

81. Zhang, Y. F., Ren, H. & Hou, Z. T. First-principles calculations of electronic and optical properties of C-doped and F, C-codoped cubic ZrO2. *J. Alloys Compd.* **617**, 86–92 (2014).

82. Tailor, H. D., Lyons, J. L., Dreyer, C. E., Janotti, A. & Van de Walle, C. G. Impact of nitrogen and carbon on defect equilibrium in ZrO2. *Acta Mater*. **117**, 286–292 (2016).

83. Griffiths, D. J. & Harris, E. G. Introduction to Quantum Mechanics. *Am. J. Phys.* **63**, 767–768 (1995).

84. Bruus, H. & Flensberg, K. *Many-Body Quantum Theory in Condensed Matter Physics: An Introduction (Oxford Graduate Texts)*. (2004).

85. Atkins, P. W. & Friedman, R. S. Molecular quantum mechanics. *Book* 545 (1997) doi:10.1002/bio.1290.

86. Sholl, D. S. & Steckel, J. A. *Density Functional Theory: A Practical Introduction*. *Density Functional Theory: A Practical Introduction* (John Wiley & Sons, Inc., 2009). doi:10.1002/9780470447710.

87. Groß, A. *Theoretical surface science: A microscopic perspective*. *Theoretical Surface Science: A Microscopic Perspective* (2009). doi:10.1007/978-3-540-68969-0.

88. Burke, K. *The ABC of DFT*. (2007).

89. Koch, W. & Holthausen, M. C. *A Chemist's Guide to Density Functional Theory*. *Journal of Physics A: Mathematical and Theoretical* vol. 44 (Wiley-VCH Verlag GmbH, 2001).

90. Mattsson, A. E., Schultz, P. A., Desjarlais, M. P., Mattsson, T. R. & Leung, K. Designing meaningful density functional theory calculations in materials science - A

primer. *Modelling and Simulation in Materials Science and Engineering* vol. 13 R1 (2005).

91. Geerlings, P., De Proft, F. & Langenaeker, W. Conceptual density functional theory. *Chem. Rev.* **103**, 1793–1873 (2003).

92. Kohn, W., Becke, A. D. & Parr, R. G. Density functional theory of electronic structure. *J. Phys. Chem.* **100**, 12974–12980 (1996).

93. Seidl, A., Görling, A., Vogl, P., Majewski, J. & Levy, M. Generalized Kohn-Sham schemes and the band-gap problem. *Phys. Rev. B - Condens. Matter Mater. Phys.* **53**, 3764–3774 (1996).

94. Himmetoglu, B., Floris, A., De Gironcoli, S. & Cococcioni, M. Hubbard-corrected DFT energy functionals: The LDA+U description of correlated systems. *Int. J. Quantum Chem.* **114**, 14–49 (2014).

95. Cococcioni, M. The LDA+U Approach: A Simple Hubbard Correction for Correlated Ground States. *Autumn Sch. Correl. Electrons, Jülich* **2**, 1–40 (2012).

96. Kryachko, E. S. Density Functional Theory and Molecular Interactions: Dispersion Interactions. in vol. 150 65–96 (Springer, Berlin, Heidelberg, 2013).

97. Anisimov, V. I., Zaanen, J. & Andersen, O. K. Band theory and Mott insulators: Hubbard U instead of Stoner I. *Phys. Rev. B* **44**, 943–954 (1991).

98. Liechtenstein, A. I., Anisimov, V. I. & Zaanen, J. Density-functional theory and strong interactions: Orbital ordering in Mott-Hubbard insulators. *Phys. Rev. B* **52**, 5467–5471 (1995).

99. Dudarev, S. L., Botton, G. A., Savrasov, S. Y., Humphreys, C. J. & Sutton, A. P. Electron-energy-loss spectra and the structural stability of nickel oxide: An LSDA+U study. *Phys. Rev. B* **57**, 1505–1509 (1998).

100. Perdew, J. P., Burke, K. & Ernzerhof, M. Generalized gradient approximation made simple. *Phys. Rev. Lett.* **77**, 3865–3868 (1996).

101. Ernzerhof, M. & Scuseria, G. E. *Assessment of the Perdew-Burke-Ernzerhof exchange-correlation functional*. (1999).

102. Hujo, W. & Grimme, S. Comparison of the performance of dispersion-corrected density functional theory for weak hydrogen bonds. *Phys. Chem. Chem. Phys.* **13**, 13942–13950 (2011).

103. Berland, K., Borck, Ø. & Hyldgaard, P. Van der Waals density functional calculations of binding in molecular crystals. *Comput. Phys. Commun.* **182**, 1800–1804 (2011).

104. Lee, K., Morikawa, Y. & Langreth, D. C. Adsorption of n -butane on Cu(100), Cu(111), Au(111), and Pt(111): Van der Waals density-functional study. *Phys. Rev. B - Condens. Matter Mater. Phys.* **82**, 1–6 (2010).

105. Abe, R. Recent progress on photocatalytic and photoelectrochemical water splitting under visible light irradiation. *J. Photochem. Photobiol. C Photochem. Rev.* **11**, 179–209 (2010).

106. Li, Z., Luo, W., Zhang, M., Feng, J. & Zou, Z. Photoelectrochemical cells for solar hydrogen production: Current state of promising photoelectrodes, methods to improve their properties, and outlook. *Energy and Environmental Science* vol. 6 347–370 (2013).

107. Luryi, S. Quantum capacitance devices. *Appl. Phys. Lett.* **52**, 501–503 (1988).

108. Kliros, G. S. Quantum capacitance of graphene sheets and nanoribbons. *Graphene Sci. Handb. Size-Dependent Prop.* **183**, 171–183 (2016).

109. Opoku, F., Govender, K. K., van Sittert, C. G. C. E. & Govender, P. P. Recent Progress in the Development of Semiconductor-Based Photocatalyst Materials for Applications in Photocatalytic Water Splitting and Degradation of Pollutants. *Adv. Sustain. Syst.* **1**, 1700006 (2017).

110. Asahi, R., Morikawa, T., Ohwaki, T., Aoki, K. & Taga, Y. Visible-light photocatalysis in nitrogen-doped titanium oxides. *Science (80-.).* **293**, 269–271 (2001).

111. Kamisaka, H., Adachi, T. & Yamashita, K. Theoretical study of the structure and optical properties of carbon-doped rutile and anatase titanium oxides. *J. Chem. Phys.* **123**, 084704 (2005).

112. Meng, X. Y. *et al.* Enhanced photoelectrochemical activity for Cu and Ti doped hematite: The first principles calculations. *Appl. Phys. Lett.* **98**, 112104 (2011).

113. Deskins, N. A., Rousseau, R. & Dupuis, M. Localized electronic states from surface hydroxyls and polarons in TiO 2(110). *J. Phys. Chem. C* **113**, 14583–14586 (2009).

114. Kleiman-Shwarsctein, A. *et al.* Electrodeposited aluminum-doped α-Fe2O3 photoelectrodes: Experiment and theory. *Chem. Mater.* **22**, 510–517 (2010).

115. Valdés, Á., Qu, Z. W., Kroes, G. J., Rossmeisl, J. & Nørskov, J. K. Oxidation and photo-oxidation of water on TiO2 surface. *J. Phys. Chem. C* **112**, 9872–9879 (2008).

116. Valḱs, Á. & Kroes, G. J. First principles study of the photo-oxidation of water on tungsten trioxide (WO3). *J. Chem. Phys.* **130**, 114701 (2009).

117. Valdés, Á. & Kroes, G. J. Cluster Study of the photo-oxidation of water on rutile titanium dioxide (TiO2). *J. Phys. Chem. C* **114**, 1701–1708 (2010).

118. Skúlason, E. *et al.* Density functional theory calculations for the hydrogen evolution reaction in an electrochemical double layer on the Pt(111) electrode. *Phys. Chem. Chem. Phys.* **9**, 3241–3250 (2007).

119. Hufnagel, A. G. *et al.* Why Tin-Doping Enhances the Efficiency of Hematite Photoanodes for Water Splitting—The Full Picture. *Adv. Funct. Mater.* **28**, 1804472 (2018).

120. Chandrasekaran, S. *et al.* Tailoring the geometric and electronic structure of tungsten

oxide with manganese or vanadium doping toward highly efficient electrochemical and photoelectrochemical water splitting. *J. Mater. Chem. A* **7**, 6161–6172 (2019).

121. Wen, L. *et al.* Why does F-doping enhance the photocatalytic water-splitting performance of mBiVO4?-a density functional theory study. *New J. Chem.* **41**, 1094–1102 (2017).

122. Zhao, X., Hu, J., Yao, X., Chen, S. & Chen, Z. Clarifying the Roles of Oxygen Vacancy in W-Doped BiVO4 for Solar Water Splitting. *ACS Appl. Energy Mater.* (2018) doi:10.1021/ACSAEM.8B00559.

123. Lin, Y. *et al.* The electronic structure, optical absorption and photocatalytic water splitting of (Fe + Ni)-codoped TiO2: A DFT + U study. *Int. J. Hydrogen Energy* **42**, 4966–4976 (2017).

124. Opoku, F., Govender, K. K., van Sittert, C. G. C. E. & Govender, P. P. Understanding the synergistic effects, optical and electronic properties of ternary Fe/C/S-doped TiO2 anatase within the DFT + U approach. *Int. J. Quantum Chem.* **118**, e25505 (2018).

125. Shi, H. *et al.* Enhanced optical absorption and photocatalytic activity of anatase TiO2 through C[sbnd]Nd-codoped: A DFT+U calculations. *J. Phys. Chem. Solids* **109**, 70–77 (2017).

126. Khan, S. U. M., Al-Shahry, M. & Ingler, W. B. Efficient photochemical water splitting by a chemically modified n-TiO2. *Science (80-.).* **297**, 2243–2245 (2002).

127. Lackner, K. S. Comment on 'Efficient Photochemical Water Splitting by a Chemically Modified n-TiO2' (III). *Science (80-.).* **301**, 1673c – 1673 (2003).

128. Fujishima, A. Comment on 'Efficient Photochemical Water Splitting by a Chemically Modified n-TiO2' (I). *Science (80-.).* **301**, 1673a – 1673 (2003).

129. Murphy, A. B. Does carbon doping of TiO2 allow water splitting in visible light? Comments on 'Nanotube enhanced photoresponse of carbon modified (CM)-n-TiO2 for

efficient water splitting'. *Sol. Energy Mater. Sol. Cells* **92**, 363–367 (2008).

130. Ramin Gul, S. *et al.* materials Electronic Band Structure Variations in the Ceria Doped Zirconia: A First Principles Study. (2018) doi:10.3390/ma11071238.

131. Wood, B. C., Ogitsu, T., Otani, M. & Biener, J. First-principles-inspired design strategies for graphene-based supercapacitor electrodes. *J. Phys. Chem. C* **118**, 4–15 (2014).

132. Pak, A. J., Paek, E. & Hwang, G. S. Tailoring the performance of graphene-based supercapacitors using topological defects: A theoretical assessment. *Carbon N. Y.* **68**, 734–741 (2014).

133. Yang, G. M., Zhang, H. Z., Fan, X. F. & Zheng, W. T. Density functional theory calculations for the quantum capacitance performance of graphene-based electrode material. *J. Phys. Chem. C* **119**, 6464–6470 (2015).

134. Mousavi-Khoshdel, M., Targholi, E. & Momeni, M. J. First-Principles Calculation of Quantum Capacitance of Codoped Graphenes as Supercapacitor Electrodes. *J. Phys. Chem. C* **119**, 26290–26295 (2015).

135. Mohsin, K. M., Srivastava, A., Fahad, M. S. & Khan, M. A. Quantum Capacitance of Hybrid Graphene Copper Nanoribbon. *ECS J. Solid State Sci. Technol.* **6**, M133–M138 (2017).

136. Song, C., Wang, J., Meng, Z., Hu, F. & Jian, X. Density Functional Theory Calculations of the Quantum Capacitance of Graphene Oxide as a Supercapacitor Electrode. *ChemPhysChem* **19**, 1579–1583 (2018).

137. Clark, S. J. *et al. First principles methods using CASTEP*. www.accelrys.com/references/castep/.

138. Vanderbilt, D. Soft self-consistent pseudopotentials in a generalized eigenvalue formalism. *Phys. Rev. B* **41**, 7892–7895 (1990).

139. Pack, J. D. & Monkhorst, H. J. ‘special points for Brillouin-zone integrations’-a reply. *Phys. Rev. B* **16**, 1748–1749 (1977).

140. Ciofini, I., Adamo, C. & Chermette, H. Self-interaction error in density functional theory: A mean-field correction for molecules and large systems. *Chem. Phys.* **309**, 67–76 (2005).

141. Cococcioni, M. & De Gironcoli, S. Linear response approach to the calculation of the effective interaction parameters in the LDA+U method. *Phys. Rev. B - Condens. Matter Mater. Phys.* **71**, 035105 (2005).

142. Tolba, S. A., Gameel, K. M., Ali, B. A., Almossalami, H. A. & Allam, N. K. The DFT+U: Approaches, Accuracy, and Applications. in *Density Functional Calculations - Recent Progresses of Theory and Application* (InTech, 2018). doi:10.5772/intechopen.72020.

143. Ataei, S. S., Mohammadizadeh, M. R. & Seriani, N. Ab Initio Simulation of the Effects of Hydrogen Concentration on Anatase TiO2. *J. Phys. Chem. C* **120**, 8421–8427 (2016).

144. Purohit, R. D., Saha, S. & Tyagi, A. K. Combustion synthesis of nanocrystalline ZrO2 powder: XRD, Raman spectroscopy and TEM studies. *Mater. Sci. Eng. B Solid-State Mater. Adv. Technol.* **130**, 57–60 (2006).

145. Zhang, Y., Ji, V. & Xu, K. W. The detailed geometrical and electronic structures of monoclinic zirconia. *J. Phys. Chem. Solids* **74**, 518–523 (2013).

146. Sinhamahapatra, A., Jeon, J. P., Kang, J., Han, B. & Yu, J. S. Oxygen-Deficient Zirconia (ZrO2-x): A New Material for Solar Light Absorption. *Sci. Rep.* **6**, 1–8 (2016).

147. Youssef, M. & Yildiz, B. Hydrogen defects in tetragonal ZrO2 studied using density functional theory. *Phys. Chem. Chem. Phys.* **16**, 1354–1365 (2014).

148. Hafez, A. M., Salem, N. M. & Allam, N. K. Unravelling the correlated electronic and optical properties of BaTaO2N with perovskite-type structure as a potential candidate

for solar energy conversion. *Phys. Chem. Chem. Phys.* **16**, 18418–18424 (2014).

149. Radin, M. D., Ogitsu, T., Otani, M., Biener, J. & Wood, B. C. First-principles simulation of capacitive charging of graphene and implications for supercapacitor design. *Phys. Rev. B - Condens. Matter Mater. Phys.* 1–12 (2014) doi:10.1103/PhysRevB.91.125415.

150. Zhan, C. *et al.* Computational Insights into Materials and Interfaces for Capacitive Energy Storage. *Adv. Sci.* **4**, (2017).

151. Xin, Y. & Yu, Y. X. Possibility of bare and functionalized niobium carbide MXenes for electrode materials of supercapacitors and field emitters. *Mater. Des.* **130**, 512–520 (2017).

152. Mousavi-Khoshdel, S. M. & Targholi, E. Exploring the effect of functionalization of graphene on the quantum capacitance by first principle study. *Carbon N. Y.* **89**, 148–160 (2015).

153. Paek, E., Pak, A. J., Kweon, K. E. & Hwang, G. S. On the origin of the enhanced supercapacitor performance of nitrogen-doped graphene. *J. Phys. Chem. C* **117**, 5610–5616 (2013).

154. Pathak, A., Gangan, A. S., Ratha, S., Chakraborty, B. & Rout, C. S. Enhanced Pseudocapacitance of MoO3-Reduced Graphene Oxide Hybrids with Insight from Density Functional Theory Investigations. *J. Phys. Chem. C* **121**, 18992–19001 (2017).

155. Hohenberg, P. & Kohn, W. Inhomogeneous electron gas. *Phys. Rev.* **136**, B864 (1964).

156. Kresse, G. & Furthmüller, J. Efficiency of ab-initio total energy calculations for metals and semiconductors using a plane-wave basis set. *Comput. Mater. Sci.* **6**, 15–50 (1996).

157. Perdew, J. P. *et al.* Atoms, molecules, solids, and surfaces: Applications of the generalized gradient approximation for exchange and correlation. *Phys. Rev. B* **46**, 6671–6687 (1992).

158. Blöchl, P. E. Projector augmented-wave method. *Phys. Rev. B* **50**, 17953–17979 (1994).

159. Joubert, D. From ultrasoft pseudopotentials to the projector augmented-wave method. *Phys. Rev. B - Condens. Matter Mater. Phys.* **59**, 1758–1775 (1999).

160. Lee, K., Murray, É. D., Kong, L., Lundqvist, B. I. & Langreth, D. C. Higher-accuracy van der Waals density functional. *Phys. Rev. B - Condens. Matter Mater. Phys.* **82**, 081101 (2010).

161. He, J., Wu, E., Wang, H., Liu, R. & Tian, Y. Ionicities of boron-boron bonds in B12 icosahedra. *Phys. Rev. Lett.* **94**, 015504 (2005).

162. Xu, Z. W. *et al.* Density functional theory study on the electronic structures and related properties of Ag-doped CH3NH3PbI3 perovskite. *Results Phys.* **15**, 102709 (2019).

163. Ma, X., Wu, X., Wang, H. & Wang, Y. A Janus MoSSe monolayer: A potential wide solar-spectrum water-splitting photocatalyst with a low carrier recombination rate. *J. Mater. Chem. A* **6**, 2295–2301 (2018).

164. Wood, C. J. *et al.* Red-absorbing cationic acceptor dyes for photocathodes in tandem solar cells. *J. Phys. Chem. C* **118**, 16536–16546 (2014).

165. Philipp, H. R. & Ehrenreich, H. Chapter 4 Ultraviolet Optical Properties. in *Semiconductors and Semimetals* vol. 3 93–124 (Elsevier, 1967).

Ahmed H. Biby

M.Sc. Nanotechnology Candidate
The American University in Cairo

Research Experience & Skills

AUC | Computational Materials Group Member

- **Energy Materials Laboratory (EML) | Advisor: Prof. Nageh Allam**
  First-principles calculations for Solid-state
- **Software Packages:** VASP
  Quantum Espresso
  CASTEP
- **Current Research Focus:** Ab-initio investigation of electronic properties, optical, and thermodynamic properties of materials.
- **Capacity Building:** Active participation in the guidance of new EML members via one-to-one mentorship and orientation session delivery.

Relevant Graduate Coursework | Physics*: Quantum Mechanics, Mathematical Physics and Advanced Nanophysics;* **Nanotechnology & materials:** *Simulation & Modelling for Nanomaterials and Systems, Nanochemistry, Selected topics: Nanotechnology and Emerging Devices, and Advanced Testing & Characterization Techniques.*

Publications & Conferences

- I. Sharafeldin*, K. Gameel, A. Usama, **A. H. Biby**, and M. Soliman, "*Theoretical and DFT Analysis of the CO Adsorption Mechanism on Late Transition Metal Surfaces*", NanoWorld Conference, Boston, April **2017**.
- K. M. Gameel, I. M. Sharafeldin, A. U. Abourayya, **A. H. Biby**, N. K. Allam "*Unveiling CO adsorption on Cu surfaces: new insights from molecular orbital principles*" Physical Chemistry Chemical Physics **2018** 20 (40), 25892-25900
- B. A. Ali, **A. H. Biby**, N. K Allam "*Fullerene C76: An Unexplored Superior Electrode Material with Wide Operating Potential Window for High-Performance Supercapacitors"* ChemElectroChem **2020** 7 (7), 1672-1678.
- N. Ahmed, A. Amer, B. A. Ali, **A. H. Biby**, Y. I. Mesbah, N. K. Allam "*Boosting the cyclic stability and supercapacitive performance of graphene hydrogels via excessive nitrogen doping: Experimental and DFT insights"* Sustainable Materials and Technologies **2020** 25, e00206

- B. A. Ali, **A. H. Biby**, N. K Allam "*A Roadmap Towards the Proper Selection of Carbon Electrodes for Energy Storage Applications: Experimental And Theoretical Insights"* Sustainable Materials and Technologies, under peer-reviewing 2020
- **A. H. Biby**, S. A. Tolba, N. K Allam "*Unveiling the role of carbon defects in the exceptional narrowing of m-ZrO_2 wide-bandgap for enhanced photoelectrochemical water splitting performance"* Advanced theory and simulations, under peer-reviewing 2020

Education

AUC | The American University in Cairo, Egypt
Master of Science in Nanotechnology GPA: 3.71/4 **Spring 2020 (expected)**
Thesis title: *Nanoengineered Materials for Energy Conversion & Storage Applications: A Density Functional Theory Study*

ASU | Ain Shams University, Cairo, Egypt
Bachelor of Science in Electrical Engineering GPA: *3.59 (Distinction)* Class rank: *Top 7%* **June 2016**

Teaching Assistantship Experience

AUC | Electronics Lab for Computer Scientists and Engineers
Fall 2016- Present
AUC | General Physics Laboratories I: Mechanics, heat, and waves
Spring 2017 **AUC |** Scientific Thinking
Fall 2017-Present

TV Interviews

- Interview at TV show called "Al Bedaya" on the second Egyptian channel as a representative for Green Initiative "Biomass & Bioenergy" Workshop.
- Interview at TV show on Al Majd Channel as a representative for Ain Shams University Racing Team.

Fellowships & Awards

AUC | The American University in Cairo, Egypt

- Laboratory Instruction Fellowship
  Spring 2017 & Fall2019
- Al Ghurair STEM Scholarship
  Fall 2017- Fall 2018
- Graduate Research Grant ($ 3000)
  Spring 2018- Present
- Academic Honor for outstanding academic achievement certificate **Spring 2020**

ASU | Ain Shams University, Cairo, Egypt

- **Second place** at Ideal Student Contest at the level of Ain Shams University (April 2016).
- **First place** at Ideal Student contest at the level of Faculty of Engineering Ain Shams University (March 2016).
- **Second Place** at the Traditional Tent Competition A competition carried out during the Egyptian Universities' Youth Week 2015.
- **Second Place** at the General Information League Competition carried out by faculty of Engineering Cultural and Political Committee of the students union. (March 2015)
- **Second Place** at the General Information League Competition carried out by Ainshams University central administration of cultural committees. (April 2015)

Extracurricular Activities

- **Best Delegate** at the Economic & Social Council at ASMUN (Ain Shams Model of United Nations).
- Enactus Ain Shams University achieved the **third place** in Enactus National Competition 2015.
- **Best Marketing Idea** in ExxonMobil's Case Study (May 2014) The Case study's title was" Introducing 100% Egyptian Vehicle to the Market".

International Organizations

- Experiment e.v Bonn, Germany **fully-funded internship** by the German federal ministry for economic cooperation and development (bmz).
- **Third place** in Urban Innovation Competition (April 2015) A competition sponsored by SODIC, Embassy of Netherlands in Cairo, American University in Cairo (AUC) and Cairo University.

Volunteering & Extracurricular Activities

- **Biomass & Bioenergy Moderator** at Green Initiative (student activity at faculty of engineering Ainshams university)
- **Renewable Energy Specialist Volunteer** at 350.org Egypt (Cairo Team)
- **Former Presentation & Projects teams member** at Enactus Ainshams university
- **Economic & Social Council Delegate** at ASMUN (Ain Shams Model of United Nations)
- **Former Logistics Head** at Life Makers (student activity at Ainshams University)
- **Former Science Communicator** at Catalysis (Scientific Awareness Activity) (Student Activity Faculty of engineering Ainshams university)

- **Participated in the first EGY Science month** as a member of Catalysis which was a partner for the organizers Nabd
- **Former Participant** at Human Development (Soft Skills) at SCOPS (Student activity at faculty of pharmacology)
- **Former Participant** at Human Resources Module at MECA (student activity at faculty of engineering Ainshams university)
- **Former participant** at Supply Chain & Procurement Module at MECA (student activity at faculty of engineering Ainshams university)
- **Former Team leader** at Team 5 at ExxonMobil's case study "Introducing 100% Egyptian Vehicle to the Market"
- **Organizer** in the organization of Guinness World Records' event (Breaking the World's Record of the "Largest Vegetable Stew ") organized by Knorr Egypt and Enactus Ain Shams University

Languages

- Arabic (Native Language)
- English (Full Professional proficiency)
- French (Basics)
- German (Basics)

References

Nageh K. Allam, PhD

Professor of Materials Science and Engineering
Director, Energy Materials Laboratory
School of Sciences and Engineering (SSE)

nageh.allam@aucegypt.edu
EML Group Website

Affiliate Scientist
Research Laboratory of Electronics
Massachusetts Institute of Technology (MIT)

nkallam@mit.edu
rle Group Website

List of Publications

- **A. H. Biby**, S. A. Tolba, N. K Allam "*Unveiling the role of carbon defects in the exceptional narrowing of m-ZrO_2 wide-bandgap for enhanced photoelectrochemical water splitting performance"* Advanced theory and simulations, under peer-reviewing 2020

- B. A. Ali, **A. H. Biby**, N. K Allam "*A Roadmap Towards the Proper Selection of Carbon Electrodes for Energy Storage Applications: Experimental and Theoretical Insights"* Sustainable Materials and Technologies, under peer-reviewing 2020

- N. Ahmed, A. Amer, B. A. Ali, **A. H. Biby**, Y. I. Mesbah, N. K. Allam "*Boosting the cyclic stability and supercapacitive performance of graphene hydrogels via excessive nitrogen doping: Experimental and DFT insights"* Sustainable Materials and Technologies **2020** 25, e00206